Physica E 42 (2010) 1871–1895

Contents lists available at ScienceDirect

Physica E

journal homepage: www.elsevier.com/locate/physe

Invited Review

Photonic quasicrystalline and aperiodic structures

A.N. Poddubny *, E.L. Ivchenko

Ioffe Physical-Technical Institute, 194021 St. Petersburg, Russia

ARTICLE INFO

Article history:
Received 1 February 2010
Accepted 11 February 2010
Available online 19 February 2010

Keywords:
Photonic quasicrystals
Deterministic aperiodic structures

ABSTRACT

Discovery of quasicrystals and other deterministic aperiodic structures initiated new fields of research in solid-state photonics. In this review, we first make an overview of recently fabricated aperiodic systems, one-, two- and three-dimensional. Then we briefly discuss clarifying and supplementing definitions of binary chains, irrational cuts through higher-dimensional lattices and tiling with regular polygons or polyhedrons. A particular attention is paid to theoretical aspects of light propagation in aperiodic photonic structures, including analysis of the geometric structure factor for different systems and application of the two-wave approximation. In the main part of the article we review different aspects of the optical spectroscopy of long-range-ordered aperiodic systems, both nonresonant and resonant, and show its state of the art in reflection, transmission, absorption, photoluminescence and nonlinear optics. Emphasis is placed on resemblance and distinction between the third form of solid matter, aperiodic long-range ordered photonic structures, and conventional crystals or disordered materials.

Contents

* Corresponding author.
E-mail address: poddubny@coherent.ioffe.ru (A.N. Poddubny).

1386-9477/$ - see front matter © 2010 Elsevier B.V. All rights reserved.
doi:10.1016/j.physe.2010.02.020

1. Introduction

The concept of quasicrystal as a nonperiodic structure with perfect long-ranged order was brought in solid-state physics by Levine and Steinhardt [1]. At present it has become clear that, in addition to crystalline and amorphous materials, there exists a third form of solids which unexpectedly fills the gap between the two well-defined condensed-matter states. Moreover, this intermediate class called aperiodic deterministic structures includes not only the Fibonacci sequences and other quasicrystals which can be described by a projection onto the n-dimensional space (n=1,2,3) of an m-dimensional periodic lattice with the dimensionality $m > n$. Examples of such aperiodic structures different from quasicrystals are Thue–Morse and period-doubling sequences. The studies of aperiodic long-range-ordered systems were extended to optics in Ref. [2] where a one-dimensional (1D) quasicrystal constructed of dielectric layers forming the Fibonacci sequence was proposed. At just the same time the concept of photonic crystals was suggested by Yablonovich [3] and John [4]. Since then photonic quasicrystals and other artificial long-range-ordered aperiodic objects are arousing an increasing interest in optical spectroscopy of solids. As far as we know, the present article is the third topical review concerning quasiperiodic photonic crystals, it follows the reviews by Albuquerque and Cottam [5] and Steurer and Sutter-Widmer [6]. In the next section, Section 2, we represent typical examples of tailored aperiodic structures realized technologically and then discuss methods of classification of aperiodic structures, Section 3. In the following sections we pay a particular attention to the theoretical aspects of light propagation in aperiodic photonic structures, including the analysis of the structure factor for different systems (Section 4) and application of the two-wave approximation (Section 5). The latter allows us to interpret the optical spectra of aperiodic structures in terms of the periodic objects and underline the specific features arising due to the nonperiodicity, Section 6. An important point is that the regimes where the two-wave approximation is invalid demonstrate the properties of optical spectra, such as scaling and self-similarity (Section 7), which are forbidden for periodic structures. To illustrate 1D-structures we consider here not only the binary aperiodic optical superlattices built of two constituent layers A and B but also the recently proposed artificial objects, namely, multiple quantum-well (QW) structures consisting of identical QWs with the interwell distances taking two different values, a and b (Section 8). In the final part of the article we briefly discuss available data on linear chains of metallic spheres, Section 9.3, as well as on 2D and 3D aperiodic systems, Section 10.

2. Experimental realizations

To the best of our knowledge, deterministic aperiodic photonic structures are not existing in nature. All the available systems are artificially fabricated. In particular cases the technology permits one to create quite complex objects, with their geometrical parameters intentionally tuned to reach the desired optical properties. Since the pioneering work by Hattori et al. [7] where the first experiment on photonic quasicrystal based on Fibonacci sequence had been reported, the technology has substantially developed and many different structures are now realized experimentally. In this section we briefly review some of these real aperiodic systems leaving the detailed discussion of their properties for the rest of the paper.

2.1. One-dimensional structures

Systems where the deterministic aperiodic modulation of dielectric constant is present only in one spatial direction are termed for simplicity as *one-dimensional* photonic structures. One-dimensional systems have been studied experimentally more frequently since their fabrication is easier than that of two- and three-dimensional systems. On the other hand, they still reveal the key fundamental features of light propagation in aperiodic media. Their simplest realization, a binary aperiodic chain, is a stack of layers made of two materials A and B with different dielectric constants ε_A and ε_B, respectively. The order of layers is determined by the rule specifying the particular structure.

Fig. 1 schematically shows a structure fabricated of two polymer materials, Cellulose Acetate and Poly Vinyl Carbazole, stacked in the Fibonacci sequence [8]. Every layer of polymer was added onto the structure by the spin coating technique. The Cellulose Acetate polymer solutions were infiltrated with sulforhodamine dye, with an emission wavelength of 618 nm. Effect of the dispersion properties of this Fibonacci structure on the dye photoluminescence spectrum is discussed in Section 8.2.

Another realization is presented in Fig. 2. The structure consists of thin GaAs quantum wells (QWs) separated by AlGaAs barriers. The barriers are of two types: long (A) and short (B), with the ratio of the lengths equal to the golden mean τ and the interwell distances arranged into the Fibonacci sequence. This is an example of the *resonant* photonic quasicrystal due to a possibility of optical excitation of the quasi-two-dimensional QW excitons confined in the QWs. Its optical properties in the frequency range around the exciton resonance frequency are considered in Section 9.1.

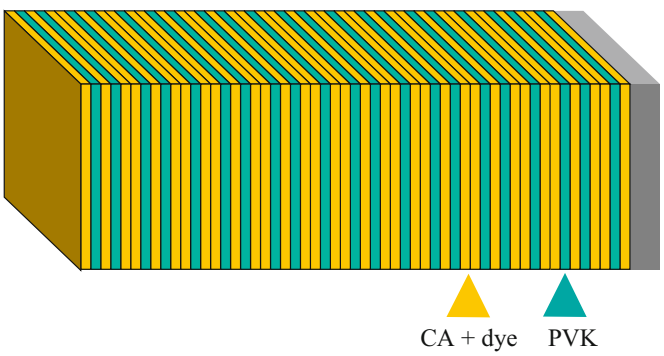

Fig. 1. Schematic illustration of the Fibonacci structure from Ref. [8]. The sample is composed of polymer layers made from Cellulose Acetate and Poly Vinyl Carbazole grown by spin-coating on the glass substrate.

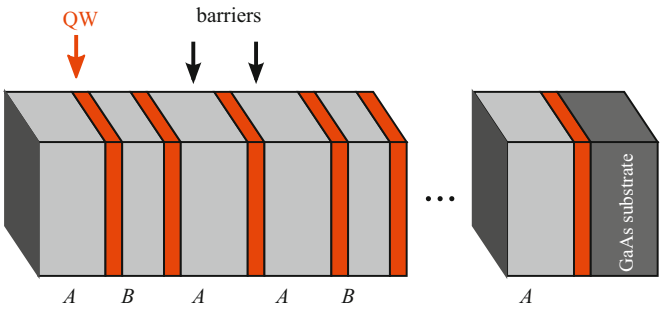

Fig. 2. Schematic illustration of the Fibonacci structure containing GaAs quantum wells sandwiched between the long (A) and short (B) AlGaAs barrier layers and realized in Refs. [9–11].

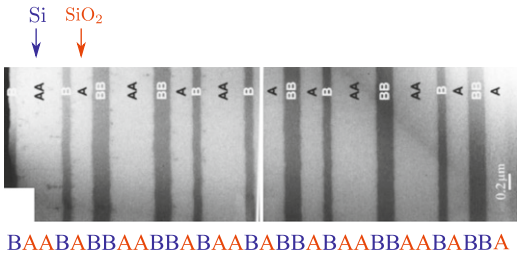

Fig. 3. TEM cross section of the 32-layer Thue–Morse structure composed of SiO_2 (layers A) and Si (layers B). From Ref. [12].

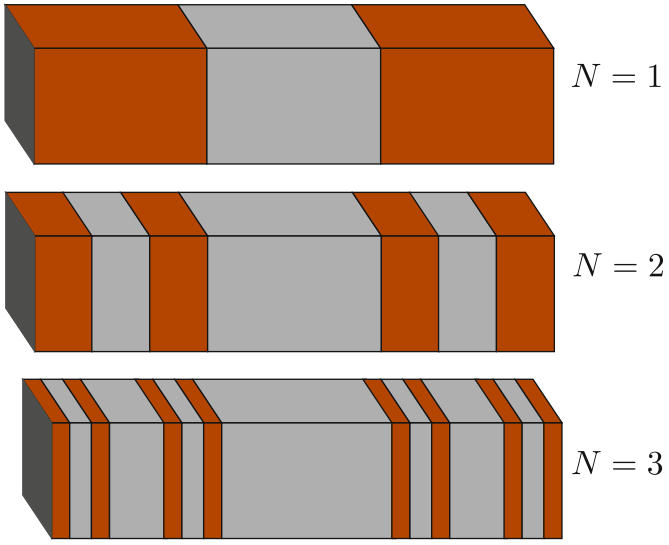

Fig. 4. Schematic illustration of Cantor multilayer structures studied in Ref. [13] for three generation numbers N=1,2,3. Dark and light colors indicate ZnS (refractive index n=2.3) and Na_3AlF_6 (n=1.34). (For interpretation of the references to color in this figure legend, the reader is referred to the web version of this article.)

Thue–Morse structures present another popular sort of one-dimensional aperiodic systems. They are deterministic but not quasicrystalline and thus principally differ from the Fibonacci binary chains. Example of such a system made of Si and SiO_2 layers and fabricated through radio-frequency magnetron sputtering on transparent fused silica substrates is shown in Fig. 3.

Fig. 4 shows fractal Cantor dielectric multilayer structures studied both experimentally and theoretically in Refs. [13–15]. The Cantor layered systems include two compositional materials, here ZnS and Na_3AlF_6. Instead of two characteristic spatial scales a and b in the binary substitutional lattices (e.g., Fibonacci and

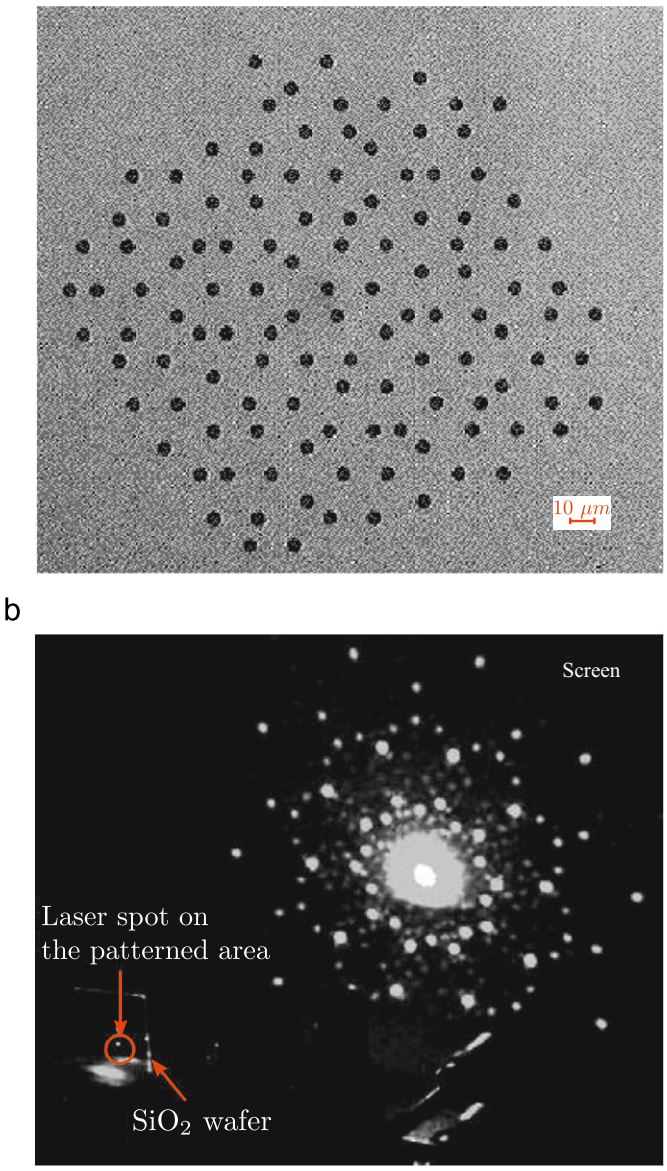

Fig. 5. (a) Micrograph of the silica sample with etched Penrose lattice of air holes, used in the diffraction experiment. (b) General photograph of the experimental diffraction pattern. From Ref. [16].

Thue–Morse chains), fractal multilayers, such as the Cantor structure, are characterized by a complex hierarchy of spatial scales.

2.2. Two-dimensional structures

Two-dimensional (2D) structures can be fabricated by etching a pattern of holes in a dielectric slab. Fig. 5(a) presents a micrograph of the Penrose-tiled photonic quasicrystal obtained by etching air cylinders in a silica substrate. Fig. 5(b) shows the photograph of the diffraction experiment. The diffraction image is characterized by the 10-fold rotational symmetry which is a characteristic feature of the Penrose lattices [1,16,18].

Quasiperiodic structures in two dimensions can possess higher degree of rotational symmetry than 2D photonic crystals. Very symmetrical diffraction pattern can be realized in the so-called *random quasicrystals* [19], see Section 10 for detailed discussion of

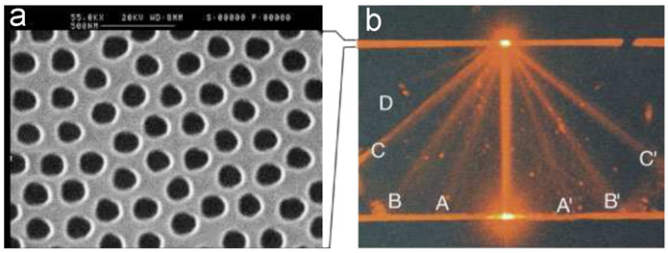

Fig. 6. (a) SEM image of a 12-fold symmetric photonic quasicrystal structure realized by etching holes in the SiN waveguide. (b) Photograph demonstrating the multiple beam diffracted reflections at the entrance face of the photonic quasicrystal. The illuminating laser wavelength is $\lambda = 630$ nm. From Ref. [17].

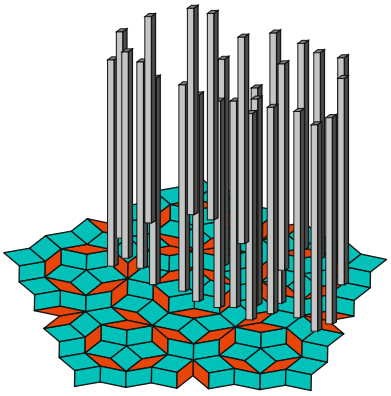

Fig. 7. Schematic illustration of the Penrose lattice of metallic rods realized in Refs. [25,26]. The metallic rods are placed at all vertices of fat and skinny rhombic cells.

these structures. Fig. 6 shows the photonic random quasicrystal structure, with macroscopic long-range 12-fold symmetry realized in Ref. [17]. Right panel of the figure demonstrates the laser beam diffraction at the entrance face of the fabricated sample. Microcavities based on two-dimensional photonic quasicrystals are also designed [20] and lasing effect from such structures has been already observed [21].

Since the pioneering works by Pendry [22], a rapt attention of researchers has been focused on the photonic structures with metallic components. One of the goals of these studies is fabrication of an artificial metal-like metamaterial with controllable plasmon frequency [23], promising for the negative-refracting materials [24]. The quasicrystalline counterpart of such systems has been analyzed in Refs. [25,26] and is schematically indicated in Fig. 7. The fabricated Penrose structures consisted of 236 cylindrical copper rods. The side of each rhombus was equal to 1.2 cm, so that the plasmon-like cutoff and the photonic band gap were observed in GHz spectral range. All these studies of artificial metallic structures, based on the light interaction with plasmon resonances, are a subject of the new rapidly emerging area of research—*plasmonics*. One of the interesting phenomena in plasmonics is the light transmission through sub-wavelength size aperture in metallic film, enhanced by plasmon excitation [27]. This effect has been observed not only for the single aperture and periodic aperture arrays, but also in case of quasicrystalline arrangement of the apertures [28–31]. Indeed, the Bragg diffraction in a quasicrystal can lead to the surface plasmon excitation as well as in the periodic lattice. Moreover, the phenomenon of enhanced transmission can be made almost independent of the polarization of the incident wave, due to the high orientational order of the quasicrystal [30]. Light transmission through one-dimensional Fibonacci and periodic sub-wavelength slit arrays was studied in Ref. [31]. The scheme of the transmission experiment [29] through the stainless steel foil patterned with 12-fold random quasicrystalline hole array is sketched in Fig. 8. It has been demonstrated in Ref. [29] that THz transmission spectra of the 2D quasiperiodic structures demonstrate distinctive sharp transmission resonances, absent in case of random apertures. Two-dimensional deterministic aperiodic arrays (Fibonacci, Thue–Morse, Rudin–Shapiro) of gold nanoparticles were fabricated on quartz substrates by electron beam lithography in Ref. [32]. Highly localized plasmonic fields in this system are optimal for surface-enhanced Raman scattering spectroscopy.

2.3. Three-dimensional structures

Structures with the quasiperiodic order arranged in all three spatial dimensions have been fabricated only recently by Man et al. [33] with a stereolithography machine (in microwave spectral range) and Ledermann et al. [34] by using the direct laser writing technique (in optical spectral range). Fig. 9 shows fabricated three-dimensional (3D) quasicrystal with the icosahedral symmetry [34]. Another

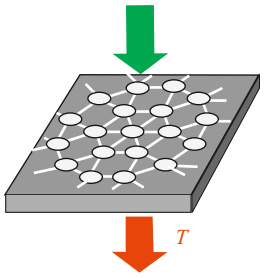

Fig. 8. Scheme of the transmission experiment [29] through the array of holes in a metallic film, arranged in quasicrystalline lattice with the long-range 12-fold symmetry.

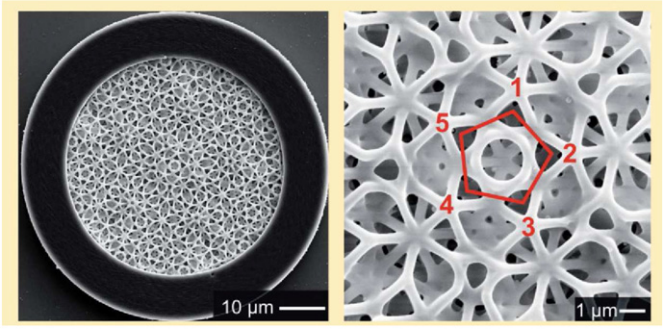

Fig. 9. Electron micrographs of fabricated 3D icosahedral quasicrystal structures. Left panel: normal view of the sample, right panel: micrograph in the larger scale. From Ref. [37].

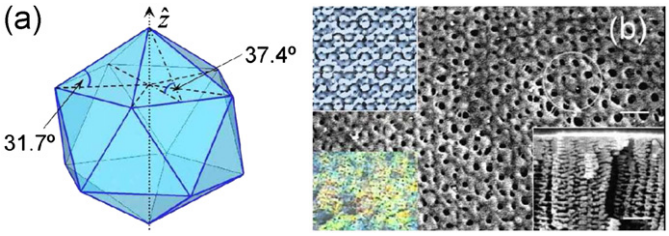

Fig. 10. (a) Illustration of icosahedral quasicrystal lattice. (b) SEM image of the fivefold symmetry in the fabricated icosahedral quasicrystal. The circle in Fig. (b) shows the fivefold symmetry. The lower-right inset in (b) is the cross-sectional SEM image of the sample. The lower-left inset, size 60 μm × 80 μm, in (b) is a fivefold normal reflection image. The scale bar in Fig. (b) is 1 μm. From Ref. [35].

realization of 3D icosahedral quasicrystal by optical interference holography technique has been reported in Ref. [35]. Schematic illustration of the icosahedral unit cell is presented in Fig. 10(a), SEM image of the sample is shown in Fig. 10(b). The lasing effect from dye-doped icosahedral quasicrystals has been observed in Ref. [36].

3. Classes of one-dimensional aperiodic systems

In short, a quasicrystal is defined as a partial projection of points of a periodic lattice in the m-dimensional hyperspace onto n-dimensional space ($n=1,2,3; m>n$). Here, in the first two subsections we present, in addition to this cut-and-project method, two other methods to classify the 1D-quasicrystals. In the third subsection we give examples of other kinds of aperiodic 1D sequences.

3.1. One-dimensional quasicrystals

There are three equivalent definitions of the quasicrystalline systems: (i) the incommensurate chains, (ii) the substitution rules and (iii) the cut-and-project method. The *incommensurate chains* and related structures [38,39] are studied since 1960s, even before the term "quasicrystal" was introduced in Ref. [1]. For 1D quasicrystals, the coordinates of the chain sites are written in the form

$$z_j = z_0 + j\overline{d} + r(j), \tag{1}$$

where $\overline{d}$ is the mean period of the 1D lattice of sites, z_0 is an arbitrary shift of the lattice as a whole, and the modulation $r(j)$ is the periodic function

$$r(j) = \Delta\left\{\frac{j}{t}+\varphi\right\}, \tag{2}$$

$\{x\}$ stands for the fractional part of x; Δ, t and φ are the structure parameters, with t being irrational and φ being noninteger. At vanishing Δ Eqs. (1) and (2) specify a simple periodic lattice with the period $\overline{d}$. In case of rational t, the structure is still periodic but has a compound supercell, whereas for irrational values of t Eq. (1) leads to a deterministic aperiodic chain termed also as "modulated crystal" [40]. The parameter Δ describes the modulation strength and the value of φ specifies the initial phase of the function $r(j)$. For z_j defined according to Eqs. (1) and (2) the spacings $z_{j+1} - z_j$ take one of the two values,

$$a = \overline{d} + \Delta\left(\frac{1}{t}-1\right) \quad \text{and} \quad b = \overline{d} + \frac{\Delta}{t}. \tag{3}$$

Therefore, a and b satisfy the conditions

$$\Delta = b-a, \quad \overline{d} = b + \frac{a-b}{t}. \tag{4}$$

The value of Δ satisfies the conditions $b>\Delta>-a$ in order the spacings a and b to be positive. Excluding Δ in Eq. (3) one can find the relation $\overline{d} = [(t-1)b+a]/t$. Moreover, the ratio N_B/N_A of numbers of the spacings a and b in an infinite lattice is related to t by

$$\frac{N_B}{N_A} = t-1. \tag{5}$$

Under the certain conditions imposed upon the values t and φ [41,42] the arrangement of points (1) can be also obtained by the *substitution rules* acting on the building segments $\mathcal{A}, \mathcal{B}$ as follows:

$$\mathcal{A} \to \sigma(\mathcal{A}) = \mathcal{M}_1\mathcal{M}_2\ldots\mathcal{M}_{\alpha+\beta},$$

$$\mathcal{B} \to \sigma(\mathcal{B}) = \mathcal{N}_1\mathcal{N}_2\ldots\mathcal{N}_{\gamma+\delta}. \tag{6}$$

Each of the symbols $\mathcal{M}_k$ and $\mathcal{N}_k$ in the right-hand side of (6) stands for $\mathcal{A}$ or $\mathcal{B}$, α and β denote the numbers of letters $\mathcal{A}$ and $\mathcal{B}$ in $\sigma(\mathcal{A})$, and γ and δ are the numbers of $\mathcal{A}$ and $\mathcal{B}$ in $\sigma(\mathcal{B})$, respectively [43]. The correspondence between the two definitions is established by the relation $t = 1+(\lambda_1-\alpha)/\gamma$ between a value of t and indices $\alpha, \beta, \gamma, \delta$, where $\lambda_1 = (\nu+\sqrt{\nu^2+4w})/2$, $\nu = \alpha+\delta$ and $w = \beta\gamma-\alpha\delta$. For the quasicrystals w must be equal to ± 1 [44].

3.2. Fibonacci structures

The one-dimensional Fibonacci lattice, being one of the most studied quasicrystals, is determined by the substitution rule [40]

$$\mathcal{A} \to \mathcal{AB}, \quad \mathcal{B} \to \mathcal{A}. \tag{7}$$

Equivalently, it can be defined as an infinite sequence $\lim_{m\to\infty}\mathcal{F}_m$, where $\mathcal{F}_m$ is the finite Fibonacci sequence of the m-th order (m=0,1,2…) satisfying the recurrence relations

$$\mathcal{F}_m = \mathcal{F}_{m-1}\mathcal{F}_{m-2} \tag{8}$$

with the initial conditions $\mathcal{F}_1 = \mathcal{B}$ and $\mathcal{F}_2 = \mathcal{A}$. For example, one has for the 7-th order sequence

$$\mathcal{F}_7 = (\mathcal{AB}\mathcal{A}\mathcal{AB}\mathcal{A}\mathcal{BA})(\mathcal{AB}\mathcal{A}\mathcal{AB}),$$

where the brackets separate the sequences $\mathcal{F}_6$ and $\mathcal{F}_5$. The chain (8) shares the name with the Fibonacci numbers F_m due to the similar recursion rule, $F_1 = F_2 = 1$, $F_{m+1} = F_m + F_{m-1}$. When Italian mathematician Leonardo da Pisa, called Fibonacci (1180–1240), proposed his famous numbers F_m, he was not likely to foresee either quasicrystals or the impact that quasicrystals would one day have as a new form of condensed matter.

In terms of the incommensurate chains, see Eqs. (1) and (2), and the substitution rules (6) parameters of the Fibonacci structure are given by

$$t = \tau \equiv (\sqrt{5}+1)/2, \quad \varphi = 0, \quad N_A/N_B = \tau,$$

$$\alpha = \beta = \gamma = 1, \ \delta = 0; \quad w = \nu = 1, \ \lambda_1 = \tau. \tag{9}$$

If the first site is chosen at the plane z=0 then $z_0 = -b$. Here the ratio a/b is arbitrary. For a=b, the structure becomes periodic [45]. For a/b equal to the golden mean τ, it becomes the *canonical* Fibonacci chain [46]. In the noncanonical Fibonacci structures this ratio is different from 1 and τ.

The structure described by Eqs. (1), (2) can be equivalently defined by the *cut-and-project method* [47]. Sizes of the unit cell of the 2D lattice (rectangular or oblique) are determined by the ratio a/b of spacings (3). However, the order of the segments $\mathcal{A}$ and $\mathcal{B}$ is determined only by t and φ and can be obtained by the projection of the square lattice [48]. In the cut-and-project method, the Fibonacci chain is generated by projection of a stripe in the auxiliary 2D space under an irrational slope. First, let us define the square lattice in the 2D space (x_1, x_2) by

$$\boldsymbol{r}_{m_1m_2} = (a_0m_1, a_0m_2), \quad m_1, m_2 \in \mathbb{Z}, \tag{10}$$

a_0 is the lattice constant. Numbers in brackets specify the first and second Cartesian components of the 2D vector, respectively. The stripe is defined by the condition

$$x_1/\tau \le x_2 < x_1/\tau + \tau a_0, \tag{11}$$

its inclination angle α equals to

$$\alpha = \arctan 1/\tau \approx 31^0,$$

see Fig. 11. Note that the stripe width W equals to $a_0\tau^2/\sqrt{1+\tau^2}$ and, for $a_0 = \tau^{-2}\sqrt{1+\tau^2}$, it becomes unity. Then we project all the points (10) satisfying (11), i.e., lying within the stripe, to the line $r_2 = r_1/\tau$. It is easy to check that the distance between the origin

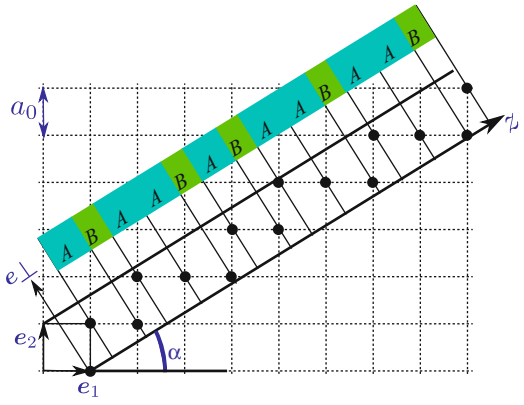

Fig. 11. Illustration of the cut-and-project method.

and the projected points is given by

$$z_j + b, \quad b = a_0 \sin\alpha = \frac{a_0}{\sqrt{1+\tau^2}}$$

with z_j given by (1), and, thus, the projected points form the Fibonacci chain.

If the stripe (11) is shifted along the vector $\boldsymbol{e}_\perp$ in Fig. 11 by a value of θW, the cut-and-project method leads to the chain given by Eq. (2) with $\varphi = -\theta$ [49,50]. Moreover, if φ can be presented as $(c_1 + c_2\tau^{-1})/c_3$, where c_i (i =1,2,3) are integers, then the infinite set of projected points preserves the self-similarity under the successive application of a finite number l of transformations (7) where l is dependent on c_i [41].

3.3. Non-Fibonacci aperiodic sequences

The generalized two-component Fibonacci lattices can be generated from the seed $\mathcal{A}$ by the substitution rule

$$\sigma_n(\mathcal{A}) \to \mathcal{A}^n\mathcal{B}, \quad \sigma_n(\mathcal{B}) \to \mathcal{A} \quad (n \geq 1) \tag{12}$$

with $\alpha = n$, $\beta = \gamma = 1$, $\delta = 0$, see Eq. (6). Since $w = \beta\gamma - \alpha\delta = 1$ they are quasicrystals described by Eqs. (1), (2) with

$$t \equiv t_n = \frac{2 - n + \sqrt{n^2+4}}{2} \quad \text{and} \quad \varphi = 0.$$

The structure with n=2 is called the silver mean lattice [51,52] with the sequence

$$\mathcal{AABAABAAABAABAAABA}\ldots$$

The infinite chain generated by Eq. (12) can also be defined as $\lim_{m\to\infty}\mathcal{S}_m$ where $\mathcal{S}_m$ is a finite sequence constructed recursively by

$$\mathcal{S}_m = \mathcal{S}_{m-1}^n\mathcal{S}_{m-2} \quad \text{with } \mathcal{S}_0 = \mathcal{B},\ \mathcal{S}_1 = \mathcal{A}. \tag{13}$$

For particular values of φ the infinite one-dimensional quasicrystal $\mathcal{S}$ described by Eqs. (1), (2) with $t = t_n$ forms a chain invariant under the operation σ_n^M, namely,

$$\sigma_n^M(\mathcal{S}) = \mathcal{S},$$

where M is an integer. For example, the chain

$$\mathcal{S} = \ldots\mathcal{S}_2^{(L)}\mathcal{S}_1^{(L)}\mathcal{S}_0^{(L)}|\mathcal{S}_1\mathcal{S}_1^{(R)}\mathcal{S}_2^{(R)}\mathcal{S}_3^{(R)}\ldots \tag{14}$$

represents a quasicrystal with t=t_2 and $\varphi = \frac{1}{4}$. Here the symbols $\mathcal{S}_m^{(L)}$ (m=0,1,2,...) and $\mathcal{S}_n^{(R)}$ (n=1,2,...) stand for the sequences

$$\mathcal{S}_m^{(L)} = \mathcal{S}_{4m+2}\mathcal{S}_{4m+1}\mathcal{S}_{4m+1}\mathcal{S}_{4m},$$

$$\mathcal{S}_n^{(R)} = \mathcal{S}_{4n-1}\mathcal{S}_{4n-2}\mathcal{S}_{4n}\mathcal{S}_{4n-1}$$

expressed via the sequences (13), the vertical line | separates two semi-infinite sequences extending to the right and to the left in

Fig. 12. Schematic illustration of invariance of the chain (14) under the transformation σ_2^4.

accordance with the following transformations:

$$\sigma_2^4\mathcal{S}_1 = (\mathcal{S}_2\mathcal{S}_1^2\mathcal{S}_0)\mathcal{S}_1(\mathcal{S}_3\mathcal{S}_2\mathcal{S}_4\mathcal{S}_3) = \mathcal{S}_0^{(L)}\mathcal{S}_1\mathcal{S}_1^{(R)},$$

$$\sigma_2^4\mathcal{S}_m^{(L)} = \mathcal{S}_{m+1}^{(L)}, \quad \sigma_2^4\mathcal{S}_n^{(R)} = \mathcal{S}_{n+1}^{(R)}.$$

As a result the aperiodic infinite chain (14) preserves self-similarity under σ_n^4 transformation [41] as illustrated in Fig. 12.

Another example of the generalization is the substitution rule $\mathcal{A} \to \mathcal{B}^{n-1}\mathcal{AB}, \mathcal{B} \to \mathcal{B}^{n-1}\mathcal{A}$. It is called the Fibonacci-class sequence of the n-th order and labelled as FC(n) [53]. Since for this sequence a value of w equals to unity it also represents a quasicrystal, $t = \lambda_1 = (n + \sqrt{n^2+4})/2$.

The substitution rule $\sigma(\mathcal{A}) = \mathcal{AB}, \sigma(\mathcal{B}) = \mathcal{A}^2$ generates the lattice known as the period-doubling sequence [6]. It is not quasicrystalline because the parameter w equals 2. Let us introduce the finite sequences $\mathcal{S}_A^{(l)} = \sigma^l(\mathcal{A})$ and $\mathcal{S}_B^{(l)} = \sigma^l(\mathcal{B})$. They satisfy the recurrence relations $\mathcal{S}_A^{(l+1)} = \mathcal{S}_A^{(l)}\mathcal{S}_B^{(l)}$ and $\mathcal{S}_B^{(l+1)} = [\mathcal{S}_A^{(l)}]^2$ with $\mathcal{S}_A^{(0)} = \mathcal{A}, \mathcal{S}_B^{(0)} = \mathcal{B}$. For the generalized substitutional rule $\mathcal{A} \to \mathcal{A}^n\mathcal{B}^m, \mathcal{B} \to \mathcal{A}$ with $m > 1$, the corresponding aperiodic lattice [54] do not belong as well to the class of quasicrystals because in this case a value of $w = m$ differs from ± 1.

Another example of non-quasicrystalline aperiodic deterministic chain is the Thue–Morse sequence introduced at the beginning of XX century [55,56]. It has recently attracted much attention due to its rich and complex spectral properties revealed in electronic [57–59], phononic [60] and photonic problems [61–66,12]. This deterministic aperiodic lattice is based on the substitution rule

$$\sigma(\mathcal{A}) = \mathcal{AB}, \quad \sigma(\mathcal{B}) = \mathcal{BA}, \tag{15}$$

starting from the initial chain $\mathcal{TM}_0 = \mathcal{A}$, and characterized by the parameters $\alpha = \beta = \gamma = \delta = 1$ and $w = 0 \neq \pm 1$. Several finite Thue–Morse sequences with the generation numbers m=0, ...,4 are given below

$$\mathcal{TM}_0 = \mathcal{A},$$

$$\mathcal{TM}_1 = \mathcal{AB},$$

$$\mathcal{TM}_2 = \mathcal{ABBA},$$

$$\mathcal{TM}_3 = \mathcal{ABBABAAB},$$

$$\mathcal{TM}_4 = \mathcal{ABBABAABBAABABBA}. \tag{16}$$

The chain $\mathcal{TM}_m$ contains $N = 2^m$ layers and has the length $L_m = 2^m\overline{d}$ ($m \geq 1$), where $\overline{d} = (a+b)/2$ is the mean layer thickness.

There are also deterministic aperiodic lattices based on four-letter $(\mathcal{A}, \mathcal{B}, \mathcal{C}, \mathcal{D})$ substitution rules, such as the Rudin–Shapiro sequence. The substitution rules for this non-quasicrystalline lattice read $\sigma(\mathcal{A}) = \mathcal{AB}$, $\sigma(\mathcal{B}) = \mathcal{AC}$, $\sigma(\mathcal{C}) = \mathcal{DB}$, $\sigma(\mathcal{D}) = \mathcal{DC}$ [6,67].

4. Structure factor

We start with writing the Maxwell equations for the electric field $\boldsymbol{E}$ of the electromagnetic wave

$$\Delta\boldsymbol{E}(\boldsymbol{r}) - \operatorname{grad}\operatorname{div}\boldsymbol{E}(\boldsymbol{r}) = -\left(\frac{\omega}{c}\right)^2\boldsymbol{D}(\boldsymbol{r}),$$

$$\operatorname{div}\boldsymbol{D}(\boldsymbol{r}) = 0, \tag{17}$$

where ω is the light frequency, c is the light velocity in vacuum and $\boldsymbol{D}$ is the displacement vector. The relation between $\boldsymbol{D}$ and $\boldsymbol{E}$ is taken in the form

$$\boldsymbol{D}(\boldsymbol{r}) = \hat{\varepsilon}(\boldsymbol{r})\boldsymbol{E}(\boldsymbol{r}) + 4\pi \boldsymbol{P}_{\rm exc}(\boldsymbol{r}). \tag{18}$$

Here $\hat{\varepsilon}(\boldsymbol{r})$ is the local nonresonant permittivity tensor and $\boldsymbol{P}_{\rm exc}(\boldsymbol{r})$ is the exciton contribution to the dielectric polarization. For a system with the dielectric response modulated only along one direction z and for the light propagating in this direction Eqs. (17) reduce to

$$\frac{d^2}{dz^2}E(z) = -\left(\frac{\omega}{c}\right)^2 [\varepsilon(z)E(z) + 4\pi P_{\rm exc}(z)]. \tag{19}$$

In the following we consider separately two particular cases of 1D photonic aperiodic systems, namely, (I) binary aperiodic optical superlattice, consisting of two types of uniform, isotropic and non-absorbing layers $\mathcal{A}$ and $\mathcal{B}$ of the thicknesses a and b with the dielectric constants ε_A and ε_B, respectively, and arranged along the z direction according to a deterministic rule, and (II) multiple quantum-well (QW) structure consisting of N identical QWs embedded in a matrix with the dielectric constant ε_b, with the interwell distances taking two values a and b. In the former case the exciton polarization is absent, $P_{\rm exc}(z) \equiv 0$, and the dielectric function is given by

$$\varepsilon(z) = \begin{cases} \varepsilon_A, & z \in \mathcal{A}, \\ \varepsilon_B, & z \in \mathcal{B}. \end{cases} \tag{20}$$

In the latter case the function $\varepsilon(z)$ is a constant ε_b and, for thin enough QWs, the excitonic dielectric response is given by

$$4\pi \boldsymbol{P}_{\rm exc}(z) = (c/\omega)^2 \chi \sum_{j=1}^{N} \delta(z - z_j)E(z), \quad \chi = \frac{2q\Gamma_0}{\omega_0 - \omega - i\Gamma}. \tag{21}$$

Here $q = n_b(\omega/c)$, ω_0 is the bare 2D-exciton resonance frequency, Γ_0 and Γ are the radiative and nonradiative exciton damping rates in a single QW structure, z_j is the center of the j-th QW (j = 1,…,N).

It follows from Eq. (21) that the optical properties of the resonant quasicrystalline chain are described by its structure factor defined by

$$f(q) = \lim_{N\to\infty} f(q,N), \quad f(q,N) = \frac{1}{N}\sum_{j=1}^{N} e^{2iqz_j}. \tag{22}$$

In the limit $N \to \infty$, the structure factor of a quasicrystal [68] consists of δ- peaks corresponding to the Bragg diffraction and characterized by two integer numbers h and h', see, e.g., Refs. [40,42],

$$f(q) = \sum_{h,h'=-\infty}^{\infty} \delta_{2q,G_{hh'}} f_{hh'}, \tag{23}$$

with the diffraction vectors

$$G_{hh'} = \frac{2\pi}{\bar{d}}\left(h + \frac{h'}{t}\right) \tag{24}$$

filling the wave-vector axis in a dense quasicontinuous way. We remind that in the periodic lattice ($\Delta = 0$) the structure factor has nonzero peaks at the single-integer diffraction vectors $G_h = 2\pi h/\bar{d}$ with $|f_h| = 1$, as shown in Fig. 13 at integer values of the dimensionless diffraction vector. One can show that, for irrational values of t and $\Delta \neq 0$, the structure-factor coefficients are given by

$$f_{hh'} = \frac{\sin S_{hh'}}{S_{hh'}} e^{i\theta_{hh'}}, \quad \theta_{hh'} = (z_0 + \Delta\{\varphi\})G_{hh'} + S_{hh'},$$

$$S_{hh'} = \frac{\pi \Delta h}{\bar{d}} + \pi h'\left(1 + \frac{\Delta}{t\bar{d}}\right) = \pi h' + \frac{\Delta}{2}G_{hh'}. \tag{25}$$

The above equations for the structure factor are valid for the arbitrary value of the phase φ in Eq. (2) and were first derived in Ref.

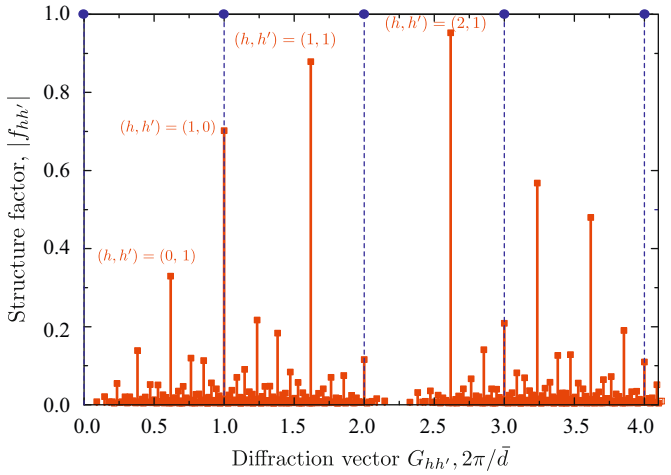

Fig. 13. Coefficients of the structure factor as a function of the diffraction vector. The lengths of dashed and solid vertical lines indicate values of $|f_h|$ and $|f_{hh'}|$ for periodic and canonic Fibonacci chains.

[10]. For the specific case when $\varphi = 0$ they can be obtained by a straightforward transformation of the result presented in Ref. [47]. Although the absolute value of the structure factor is independent of φ, the order of segments $\mathcal{A}$ and $\mathcal{B}$ in the chain determined by Eq. (1) does depend on this phase. On the other hand, Eq. (25) generalizes the results of Ref. [68] obtained for the Fibonacci lattice shifted by the phase $\varphi < 1$, to the quasicrystal with arbitrary $\bar{d}$, Δ and t.

For the canonic Fibonacci lattice, the equations for $G_{hh'}$, $\bar{d}$, $S_{hh'}$ and $\theta_{hh'}$ reduce to $\bar{d} = b(3-\tau)$,

$$G_{hh'} = \frac{2\pi}{\bar{d}}\left(h + \frac{h'}{\tau}\right), \quad \bar{d} = b + \frac{a-b}{\tau} = b\frac{1+\tau^2}{1+\tau} = b(3-\tau) \tag{26}$$

and

$$S_{hh'} = \pi\frac{\tau(\tau h' - h)}{1+\tau^2}, \quad \theta_{hh'} = \frac{\tau - 2}{\tau}S_{hh'}, \quad |f_{hh'}| = \frac{\sin S_{hh'}}{S_{hh'}}. \tag{27}$$

It should be stressed that the set of the diffraction vectors in Eq. (24) is independent of the ratio $\rho = a/b$ and coincides for the both canonical and noncanonical Fibonacci MQWs with the equal mean period $\bar{d}$. For the canonical Fibonacci structures, the largest values of $|f_{hh'}| \approx 1$ correspond to h and h' equal to the subsequent Fibonacci numbers: $(h,h') = (F_j, F_{j-1})$. For the noncanonical structures, the coefficients $|f_{hh'}|$ are maximal when ratio of h'/h is close to $a/b - 1$, as one can see from the analysis of Eqs. (25).

For the sake of completeness, we can also analyze a slightly disordered periodic structure with the long-range order maintained and the QW positions defined by

$$z_j = j\bar{d} + \delta z_j, \tag{28}$$

where the deviation δz_j is randomly distributed and defined by the vanishing average, $\langle \delta z_j \rangle = 0$, and the dispersion $\sigma_z^2 = \langle (\delta z_j)^2 \rangle$. The structure factor $f(q) = \lim_{N\to\infty} f(q,N)$ of such a lattice averaged over the disorder realizations has the form

$$\langle f(q) \rangle = \sum_h \delta_{2q,G_h} e^{-(q\sigma_z)^2/2}, \quad G_h = 2\pi h/\bar{d}. \tag{29}$$

The dispersion of $f(q, N)$ tends to zero with $N \to \infty$, and Eq. (29) provides a good estimation of the structure factor for any fixed disorder realization whenever $N \gtrsim 10$. The long-ranged correlations of QW positions are preserved by (28), and the Bragg diffraction is possible with the same diffraction vectors as in the periodic lattice. However, the structure-factor coefficients drop

drastically with the growth of σ_z. The exponential factor in (29) is equivalent to the Debye–Waller factor caused by the thermal motion of atoms in a crystalline lattice [69].

For a nonresonant canonical Fibonacci binary chain, the role of structure factor is played by the Fourier transform ε_G of dielectric constant defined by

$$\varepsilon(z)=\sum_G \varepsilon_G e^{iGz}, \quad \varepsilon_G=\frac{1}{L}\int_0^L dz\varepsilon(z)e^{-iGz}, \tag{30}$$

where L is the chain length. For the Fibonacci sequence the straightforward derivation leads to the following results:

$$\varepsilon_{-G}=Q_G(\varepsilon_A,a)f^{(A)}(G)+Q_G(\varepsilon_B,b)f^{(B)}(G), \tag{31}$$

where

$$Q_G(\varepsilon,l)=\varepsilon\frac{e^{iGl}-1}{iG\bar{d}}$$

and

$$f^{(A,B)}(G)=\lim_{N_{A,B}\to\infty}\frac{1}{N_{A,B}}\sum_{j=1}^{N_{A,B}} e^{iGz_{j_{A,B}}}=\sum_{h,h'=-\infty}^{\infty}\delta_{G,G_{h,h'}}f^{(A,B)}_{h,h'},$$

$$f^{(A)}_{hh'}=\frac{\sin(S_{hh'}/\tau)}{S_{hh'}}\exp\left[i\frac{S_{hh'}}{\tau}\left(\frac{2}{\tau}-1\right)\right], \tag{32}$$

$$f^{(B)}_{hh'}=\frac{\sin(S_{hh'}/\tau^2)}{S_{hh'}}\exp\left[i\frac{S_{hh'}}{\tau}\left(\frac{1}{\tau}-2\right)\right]. \tag{33}$$

In fact, these equations agree with the result obtained by Dharmawardana et al. [70] for the Fourier transform of the local photoelastic coefficient in the Fibonacci superlattices. Note that the sum $f^{(A)}_{hh'}+f^{(B)}_{hh'}$ reduces to the structure-factor coefficient $f_{hh'}$ in Eq. (27).

The Thue–Morse sequence is not quasicrystalline, it is characterized by a singular continuous structure factor. In the quasicrystals, the structure factor $f(q, N)$ of the chain with N layers, in the limit $N\to\infty$, either tends to zero as $1/N$ or saturates at the diffraction peaks. Although the structure factor of the Thue–Morse lattice

$$f(q,m)\equiv f(q,N_m)=\frac{1}{2^m}\sum_{j=1}^{2^m} e^{2iqz_j} \tag{34}$$

also has Bragg peaks at certain values $q = G_h/2$, its behavior in the limit $N_m=2^m\to\infty$ for other values of q is more complex:

$$|f(q,m)|\propto\frac{1}{(N_m)^{\alpha(q)}}=2^{-m\alpha(q)}, \tag{35}$$

where $\alpha(q)$ is the wavevector-dependent scaling index. Below we discuss some properties of the structure factor found in Refs. [57,60,71].

It is convenient to introduce an auxiliary sequence $\widetilde{\mathcal{TM}}_m$ obtained from $\mathcal{TM}_m$ by the interchange of the segments $\mathcal{A}$ and $\mathcal{B}$, e.g., $\widetilde{\mathcal{TM}}_1=\mathcal{BA}$. The definition (15) implies the recurrence rule

$$\mathcal{TM}_{m+1}=\mathcal{TM}_m\widetilde{\mathcal{TM}}_m, \quad \widetilde{\mathcal{TM}}_{m+1}=\widetilde{\mathcal{TM}}_m\mathcal{TM}_m. \tag{36}$$

Consequently, we can obtain recurrence relations for the structure factors $f(q,m)$ and $\tilde{f}(q,m)$ of the sequences $\mathcal{TM}_m$ and $\widetilde{\mathcal{TM}}_m$, respectively:

$$f(q,m+1)=\frac{f(q,m)+e^{2iqL_m}\tilde{f}(q,m)}{2},$$

$$\tilde{f}(q,m+1)=\frac{\tilde{f}(q,m)+e^{2iqL_m}f(q,m)}{2} \tag{37}$$

with $f(q,1) = (1 + e^{2iqa})/2$ and $\tilde{f}(q,1)=(1+e^{2iqb})/2$. Solving Eqs. (37) we obtain

$$f(q,m)=e^{iq\bar{d}(2^m-2)}(\Pi^+_m f^+ +\Pi^-_m f^-), \tag{38}$$

where $f^{\pm}=[f(q,1)\pm\tilde{f}(q,1)]/2$ and the products

$$\Pi^+_m=\prod_{l=1}^{m-1}\cos(2^l q\bar{d})=2^{1-m}\frac{\sin(2^m qd)}{\sin(2q\bar{d})}$$

and

$$\Pi^-_m=(-i)^{m-1}\prod_{l=1}^{m-1}\sin(2^l q\bar{d}),$$

describe, respectively, the Bragg and non-Bragg diffraction. In the limit $N_m\to\infty$ the first product tends to equidistant Bragg peaks,

$$\lim_{N_m\to\infty}\Pi^+_m=\sum_{h=0}^{\infty}\delta_{2q,G_h}, \quad G_h=\frac{\pi h}{\bar{d}}. \tag{39}$$

They originate from the periodic subset of the Thue–Morse lattice sites with the period $2\bar{d}=a+b$. The structure-factor magnitude at the peaks G_h is given by [71]

$$|f_h|=\cos^2\left(\frac{\pi ah}{2\bar{d}}\right)=\cos^2\left(\frac{\pi bh}{2\bar{d}}\right). \tag{40}$$

The second product $\Pi^-_m(q)$ is specific to the Thue–Morse sequence. It tends to zero when $N_m\to\infty$ but has much more rich spectral behavior than $\Pi^+_m(q)$. The overall picture of structure factor is shown in Fig. 14. The figure demonstrates that only the Bragg peaks at integer $2q\bar{d}/\pi$ survive in long sequences. Between the Bragg peaks the value of $\Pi^+_m(q)$ decays rapidly as 2^{-m} and an additional slowly decaying self-similar pattern is represented by the product $\Pi^-_m(q)$.

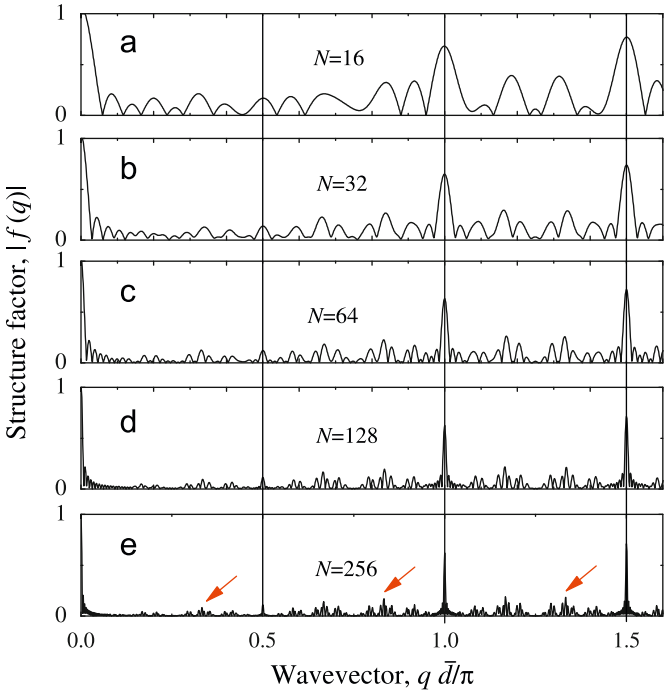

Fig. 14. Structure factor $|f(q,m)|$ of the Thue–Morse chains. Panels (a)–(e) correspond to the chains $\mathcal{TM}_4,\ldots,\mathcal{TM}_8$ containing N = 16, …, N=256 layers, respectively. Inclined arrows in the panel (e) indicate the values of $q\bar{d}=\pi/3,5\pi/6,4\pi/3$, where the scaling index of the structure factor is smallest.

The scaling index $\alpha(q)$ characterizes the behavior of $\Pi_m^-(q)$ at $N_m \to \infty$ and can be expressed in the form

$$\alpha(q) = -\lim_{N_m\to\infty} \frac{1}{m\ln 2} \sum_{l=1}^{m-1} \ln|\sin(2^l q\overline{d})|. \quad (41)$$

For most values of q the scaling index is unity, $\alpha(q) \equiv 1$. This follows from the replacement of summation in (41) by integration and the identity $\int_0^1 \ln\sin(\pi x)\,dx = -\ln 2$. The minimum value of the scaling index is

$$\min[\alpha(q)] = \alpha(\pi/3\overline{d}) = -\frac{\ln(\sqrt{3}/2)}{\ln 2} \approx 0.21. \quad (42)$$

One can obtain this relation taking into account that, at $q = \pi/(3\overline{d})$, the absolute values of all sine functions in (41) are equal to $\sqrt{3}/2$. The key property of the scaling index

$$\alpha(q) = \alpha\left(q + \frac{2^n\pi}{\overline{d}}\right) \quad (n = 0, \pm 1, \pm 2, \ldots)$$

leads to a complex hierarchic structure of the function $\alpha(q)$. For example, the scaling indices for the three wave vectors $q = \pi/(3\overline{d}), 5\pi/(6\overline{d}), 4\pi/(3\overline{d})$ indicated by inclined arrows in Fig. 14(e) are all equal to 0.21. The limit of $\alpha(q)$ at $N_m \to \infty$ exists for any rational $q\overline{d}/\pi$. This property follows from the fact that, for rational qd/π, the sequence $2^l q\overline{d} \bmod \pi$ should reach cycle at some integer l. The limit in Eq. (41) does not exist for certain irrational values of $q\overline{d}/\pi$ [57].

In concluding this section, we briefly emphasize the relation between 1D quasicrystalline and non-quasicrystalline deterministic systems. We remind that, concerning the arrangement of elementary units, 1D quasicrystals can be obtained from 2D lattices by one of the three above-mentioned methods, the cutting and projecting, introducing the incommersurate chains (1) or the substitution rules (6) with $w = \beta\gamma - \alpha\delta = \pm 1$. As far as we know, there exists no self-consistent constructive definition of the geometry of non-quasicrystalline deterministic systems. Their properties are revealed from comparison of the structure factors. In quasicrystals, the structure factor $f(q, N)$, see Eq. (22), tends with $N \to \infty$ to a sum of countably many of delta peaks at the dense set of wave vectors characterized by pairs of two arbitrary integers. The analysis of Thue–Morse and period-doubling sequences [71] shows that the structure factor of non-quasicrystalline long-range ordered chains has the Bragg peaks at the equidistant points q enumerated by one integer and, in addition, the singular peaks whose amplitude decrease with increasing the number of units N as N^α with the scaling index $\alpha < 1$. Note that for a disordered system, at any q, the structure factor $f(q, N)$ goes down with $N \to \infty$ with the scaling index $\alpha = 1$. Thus, the non-quasicrystalline deterministic systems fall into a middle ground between crystalline and disordered systems. Interestingly, in its turn the gap between the Thue–Morse sequences and completely disordered systems is filled by randomized Markov versions of Thue–Morse photonic sequences [72]. The Markov Thue–Morse sequence is defined by the conditional probabilities $P_{AB|A} = P_{AB|B} = 1$ and $P_{AB|A} = P_{AB|B} = P_{BA|A} = P_{BA|B} = 1/2$, where $P_{M_1M_2|M_3}$ is the probability to have the layer M_3 after the pair of layers M_1 M_2. This is the short-range order which is preserved in the conventional, long-range ordered, Thue–Morse chain.

5. Light dispersion in the two-wave approximation

In this and next sections we apply the two-wave approximation to derive the light dispersion and the reflectivity spectra of the aperiodic multilayered structures. The electric field of the light wave propagating in the multilayered structure satisfies the following wave equation

$$\left(-\frac{d^2}{dz^2} - q^2\right) E(z) = 2q \sum_G e^{iGz} P_G E(z), \quad (43)$$

where $E(z)$ is the electric field of the light wave at the frequency ω [the real field $E(z, t)$ is defined as $E(z)e^{-i\omega t} + \text{c.c.}$], G are the reciprocal vectors G_h in the case of a periodic structure and the diffraction vectors $G_{hh'}$ in the case of a photonic quasicrystal, the wave vector q and coefficients P_G are defined by

$$q = \frac{\omega}{c}\sqrt{\bar{\varepsilon}}, \quad P_G = \frac{q}{2}\frac{\varepsilon_G}{\bar{\varepsilon}} \quad (44)$$

for the nonresonant Fibonacci lattice (case I) and by

$$q = \frac{\omega}{c}\sqrt{\varepsilon_b}, \quad P_G = \xi f^*_{hh'} \quad (45)$$

for the case II $\xi = \chi/(2q\overline{d})$, χ and $f_{hh'}$ are introduced in Eqs. (21) and (25), and $\bar{\varepsilon}$ is the average dielectric constant

$$\bar{\varepsilon} = \frac{\varepsilon_A N_A a + \varepsilon_B N_B b}{N_A a + N_B b} = \frac{\varepsilon_A(\tau+1) + \varepsilon_B}{\tau + 2}. \quad (46)$$

Note that, in the absence of dissipation, $P_{-G} = P_G^*$, and in the case I the coefficient P_0 reduces to zero. Eq. (43) allows one to write the electro-magnetic field in the structure as a superposition of the "Bloch-like" waves

$$E_K(z) = \sum_G e^{i(K-G)z} E_{K-G}. \quad (47)$$

The difference $K_1 - K_2$ for two different waves $E_{K_1}(z)$ and $E_{K_2}(z)$ in the set (47) cannot be an integer number of any diffraction vector G. Moreover, for unambiguity the dispersion $\omega_{K'}$ with K' being the real part of K is defined in the extended-zone scheme where, for positive K', $\omega_{K'}$ is a monotonously increasing function of K'. Note that, for a 1D system, the integrated density of states, $\rho(\omega_2, \omega_1)$, with the frequencies ω lying in the interval between ω_2 and ω_1 is proportional to the difference $K(\omega_2) - K(\omega_1)$ of the light wave vectors K. This can be demonstrated as follows:

$$\int_{\Omega_1}^{\Omega_2} d\omega \sum_K \delta(\omega - \omega_K) = \frac{L}{2\pi}\int_{\Omega_1}^{\Omega_2} \frac{d\omega}{d\omega_K/dK} = \frac{L}{2\pi}\int_{\Omega_1}^{\Omega_2} d\omega \frac{dK(\omega)}{d\omega} = \frac{L}{2\pi}[K(\Omega_2) - K(\Omega_1)]. \quad (48)$$

In the *two-wave approximation*, only two space harmonics K and $K' = K - G$ are taken into consideration in the superposition (43) and the electric field is approximately written as

$$E(z) = E_K e^{iKz} + E_{K-G} e^{i(K-G)z}. \quad (49)$$

Then the exact wave equation (43) is reduced to a system of two coupled equations

$$(q^2 - K^2 + 2qP_0)E_K + 2qP_G E_{K-G} = 0,$$

$$2qP_{-G}E_K + [q^2 - (K-G)^2 + 2qP_0]E_{K-G} = 0. \quad (50)$$

We analyze a narrow frequency region near the Bragg frequency ω_G satisfying the condition

$$q(\omega_G) = \frac{G}{2} \quad (51)$$

and assume $K \approx G - K \approx q(\omega) \approx q(\omega_G)$. This allows one to reduce Eqs. (50) to

$$(q - K + P_0)E_K + P_G E_{K-G} = 0,$$

$$P_{-G}E_K + (q + K - G + P_0)E_{K-G} = 0. \quad (52)$$

The two eigenvalues K corresponding to the frequency ω satisfy the dispersion equation

$$(q - K + P_0)(q + K - G + P_0) = P_G P_{-G} \quad (53)$$

and are given by

$$K=\frac{G}{2}\pm Q,\quad Q=\sqrt{\left(q-\frac{G}{2}+P_0\right)^2-P_G P_{-G}}. \tag{54}$$

First, we take the coefficients P_G to be frequency-independent and $P_0=0$. Then the energy spectrum has around ω_G a band gap with the edges ω_+ and ω_- spaced by

$$\Delta\equiv\omega^+-\omega^-=\frac{2c|P_G|}{\sqrt{\bar{\varepsilon}}} \tag{55}$$

and centered at the frequency

$$\overline{\omega}\equiv\frac{\omega_++\omega_-}{2}=\frac{c}{\sqrt{\bar{\varepsilon}}}\frac{G}{2}. \tag{56}$$

We recall that the energy flux density $\boldsymbol{S}$ for the light wave is given by the standard equation $(c/4\pi)\boldsymbol{E}\times\boldsymbol{B}$, where $\boldsymbol{B}$ is the magnetic field and c is the light velocity in vacuum. For the wave (49) one has

$$S_z=\frac{c^2}{4\pi\omega}\mathrm{i}\left[E(z)\frac{dE^*(z)}{dz}-E^*(z)\frac{dE(z)}{dz}\right]=\frac{c^2}{2\pi\omega}\left[K'|E_K|^2+(K'-G)|E_{K-G}|^2\right]$$

or, otherwise,

$$S_z=\frac{c^2}{2\pi\omega}\left[Q'(|E_K|^2+|E_{K-G}|^2)+\frac{G}{2}(|E_K|^2-|E_{K-G}|^2)\right],$$

where $K'=\mathrm{Re}\{K\}$, $Q'=\mathrm{Re}\{Q\}$. In the gap, Q is imaginary and $|E_K|^2=|E_{K-G}|^2$ because, according to Eq. (52),

$$\left(q-Q-\frac{G}{2}+P_0\right)P^*_{-G}|E_K|^2=\left(q+Q^*-\frac{G}{2}+P_0\right)P_G|E_{K-G}|^2.$$

If the Fourier components have a pole at the frequency ω_0,

$$P_G(\omega)=\frac{p_G}{\omega_0-\omega-\mathrm{i}\Gamma}, \tag{57}$$

and, in addition, the resonant Bragg condition

$$\frac{\omega_0}{c}n_b=\frac{G}{2} \tag{58}$$

is satisfied then the structure is characterized by two symmetrical exciton–polariton band gaps. The edges, $\omega^{\pm}_{\mathrm{out}}$ and $\omega^{\pm}_{\mathrm{in}}$, of these band gaps are obtained from Eq. (53) by setting $K=G/2$ or, equivalently, $Q=0$. The result reads (for $\Gamma\to+0$)

$$\omega^{\pm}_{\mathrm{out}}=\omega_0\pm\sqrt{\frac{c}{n_b}(p_0+|p_G|)},\quad \omega^{\pm}_{\mathrm{in}}=\omega_0\pm\sqrt{\frac{c}{n_b}(p_0-|p_G|)}. \tag{59}$$

In the resonant periodic Bragg structures, the values of p_0, p_G and p_{-G} coincide and the system has a single gap of the width

$$\Delta=2\sqrt{\frac{2cp_0}{n_b}}.$$

In a quasicrystal, $|p_G|$ with $G\neq0$ is smaller than p_0 and the system has two gaps of the equal widths

$$|\omega^{\pm}_{\mathrm{out}}-\omega^{\pm}_{\mathrm{in}}|=\sqrt{\frac{c}{n_b}}\left(\sqrt{p_0+|p_G|}-\sqrt{p_0-|p_G|}\right).$$

Particularly, in a resonant Bragg QW quasicrystal with the Fibonacci sequence, the coefficients P_0, P_G, P_{-G} are equal to $\xi,\xi f^*_{hh'},\xi f_{hh'}$, respectively, and Eq. (59) is rewritten as

$$\omega^{\pm}_{\mathrm{out}}=\omega_0\pm\Delta\sqrt{\frac{1+|f_{hh'}|}{2(h+h'/\tau)}},$$

$$\omega^{\pm}_{\mathrm{in}}=\omega_0\pm\Delta\sqrt{\frac{1-|f_{hh'}|}{2(h+h'/\tau)}}. \tag{60}$$

6. Reflection and transmission in the two-wave approximation

6.1. Reflection from a semi-infinite structure

For simplicity we first consider the light reflection from a semi-infinite multilayered structure formed by layers $\mathcal{A}$ and $\mathcal{B}$ and ignore the frequency dependence of the coefficients P_G. Then we turn to a finite aperiodic sequence sandwiched between the semi-infinite layers of the material A and also consider consequences of the resonant frequency dependence of P_G.

In order to derive an analytical expression for the reflection coefficient we can write the field in the two regions, the left semi-infinite homogeneous layer $\mathcal{A}$ and the semi-infinite sequence of the layers $\mathcal{A}$ and $\mathcal{B}$, in the following form:

$$E(z)=\begin{cases}E_0\mathrm{e}^{\mathrm{i}qz}+E_r\mathrm{e}^{-\mathrm{i}qz} & (z<0),\\ E_K\mathrm{e}^{\mathrm{i}Qz}\left(\mathrm{e}^{\mathrm{i}Gz/2}+\zeta\mathrm{e}^{-\mathrm{i}Gz/2}\right) & (0<z).\end{cases} \tag{61}$$

Here E_0 and E_r are the amplitudes of the incident and reflected waves, E_K is the amplitude introduced in Eq. (49), and

$$\zeta=\frac{E_{K-G}}{E_K}=-\frac{P_{-G}}{q+K-G+P_0}.$$

The amplitude reflection coefficient is defined by

$$r=\frac{E_r}{E_0}.$$

Values of r and E_K/E_0 can be found by imposing the boundary conditions which are continuity of the electric field $E(z)$ and its first derivative $dE(z)/dz$ at the point $z=0$ and reduce to

$$E_0+E_r=E_K+E_{K-G},\quad q(E_0-E_r)=KE_K+(K-G)E_{K-G}. \tag{62}$$

One can readily check that, for these boundary conditions, the energy flux S_z is conserved. It follows from Eqs. (62) that the reflection coefficient satisfies the equation

$$\frac{\omega}{c}n_A\frac{1-r}{1+r}=\frac{K+(K-G)\zeta}{1+\zeta}$$

and, therefore, one has

$$r=-\frac{n_{\mathrm{eff}}-n_A}{n_{\mathrm{eff}}+n_A}, \tag{63}$$

$$n_{\mathrm{eff}}=\frac{c}{\omega}\frac{K+(K-G)\zeta_G}{1+\zeta_G}=\frac{c}{\omega}\left(K-\frac{G}{2}+\frac{G}{2}\frac{1-\zeta_G}{1+\zeta_G}\right).$$

Taking into account that within the gap $|\zeta_G|=1$, so that ζ_G can be presented as a phase factor $\mathrm{e}^{\mathrm{i}\Phi}$, we conclude that, in the gap frequency region where $Q=K-(G/2)$ is pure imaginary, the effective refractive index n_{eff} is also imaginary and $|r|=1$.

6.2. Reflection from a structure of finite thickness

For an aperiodic structure of the thickness L sandwiched between the semi-infinite layers of material A, the electric field is described in an analytical form in the three regions as follows:

$$E(z)=\begin{cases}E_0\mathrm{e}^{\mathrm{i}qz}+E_r\mathrm{e}^{-\mathrm{i}qz} & (z<0),\\ E_{K_+}\mathrm{e}^{\mathrm{i}Qz}(\mathrm{e}^{\mathrm{i}Gz/2}+\zeta_+\mathrm{e}^{-\mathrm{i}Gz/2})+E_{K_-}\mathrm{e}^{-\mathrm{i}Qz}(\mathrm{e}^{\mathrm{i}Gz/2}+\zeta_-\mathrm{e}^{-\mathrm{i}Gz/2}) & (0<z<L),\\ E_t\mathrm{e}^{\mathrm{i}q(z-L)} & (L<z).\end{cases} \tag{64}$$

Here E_t is the amplitude of the transmitted wave, $E_{K_\pm}$ are the amplitudes E_K in Eq. (49) for the wave vectors $K_\pm=(G/2)\pm Q$, and

$$\zeta_\pm=\frac{E_{K_\pm-G}}{E_{K_\pm}}=-\frac{P_{-G}}{q+K_\pm-G+P_0}.$$

The boundary conditions at $z=0$ and $z=L$ relate the electric field amplitudes

$$E_0+E_r=(1+\zeta_+)E_{K_+}+(1+\zeta_-)E_{K_-},$$

$$q(E_0-E_r)=\sum_{m=\pm}[K_m+(K_m-G)\zeta_m]E_{K_m},$$

$$E_t=\sum_{m=\pm}e^{iK_mL}(1+\zeta_m e^{iGL})E_{K_m},$$

$$qE_t=\sum_{m=\pm}e^{iK_mL}[K_m+(K_m-G)\zeta_m e^{iGL}]E_{K_m}. \quad (65)$$

If the number N of wells in the Fibonacci QW structure coincides with F_j+1, where F_j is one of the Fibonacci numbers, then the product $G_{hh'}L$ differs from an integer multiple of 2π by a negligibly small value,

$$\delta_N=-G_{hh'}s(1-\tau)^{j-1}\tau^{-2}\frac{h-\tau h'}{h+\tau^{-1}h'}.$$

In this case the phase factor $\exp(iG_{hh'}L)$ and the length L can be replaced, respectively, by unity and the product $N\bar{d}$ ($\bar{d}$ is the average interwell distance). The straightforward derivation results in surprisingly simple expressions for the reflection and transmission coefficients,

$$r_N=\frac{\xi f_{hh'}}{(G/2)-q-\xi-iQ\cot(QN\bar{d})},$$

$$t_N=-\frac{iQ}{\xi f_{hh'}\sin(QN\bar{d})}r_N. \quad (66)$$

For nonresonant Fibonacci chain the Bragg condition (51) reduces to

$$\frac{\omega_G\sqrt{\bar{\varepsilon}}}{c}\bar{d}=\pi\left(h+\frac{h'}{\tau}\right), \quad (67)$$

where $\bar{\varepsilon}$ is the average dielectric constant (46). The solution of Eqs. (64) results in the following expressions for the reflection and transmission coefficients:

$$r_N=\frac{P_G}{(G/2)-q-iQ\cot(QN\bar{d})},$$

$$t_N=-\frac{iQ}{P_G\sin(QN\bar{d})}r_N. \quad (68)$$

6.3. Calculation of optical spectra

In this subsection we will use the two-wave approximation to analyze light reflection from the Fibonacci binary chains. As the first illustration, we present in Fig. 15 the dispersion of light wave and the reflectivity calculated in this approximation for the semi-infinite Fibonacci sequence of the dielectric layers $\mathcal{A}$ and $\mathcal{B}$. The parameters of the structure are as follows: $n_A=1$, $n_B=\tau$, $a/b=\tau$. The solid curve in Fig. 15(a) represents the close-to-exact calculation in which 12 plane waves are included in the expansion (47). For the first time, the light dispersion analysis of light waves in Fibonacci photonic quasicrystals using a large but finite number of main diffraction vectors G has been performed by Kaliteevski et al. in Ref. [73]. For comparison, the dashed and dotted curves in Fig. 15(a) are calculated in the two-wave approximation where the mixing of two plane waves, either K and $K-G_{1,-1}$ or K and $K-G_{1,0}$ are taken in consideration. One can see that the two-wave approximation successfully describes the light dispersion in the anticrossing region around the frequency $\bar{\omega}$ defined by Eq. (56). Fig. 15(b) shows the reflection spectra calculated by using Eq. (68) independently for $G=G_{1,-1}$ and $G=G_{1,0}$. As expected the reflectivity inside each band gap is constant and equal to unity.

Fig. 16 shows the reflectivity and transmittivity of the structure containing a finite number, $F_{11}=89$, layers $\mathcal{A}$ and $\mathcal{B}$ arranged in the Fibonacci sequence. Other parameters are the same as those used in the calculation of curves in Fig. 15. The positions of maxima in the reflection spectrum and minima in the transmission spectrum correlate with the gaps obtained in the

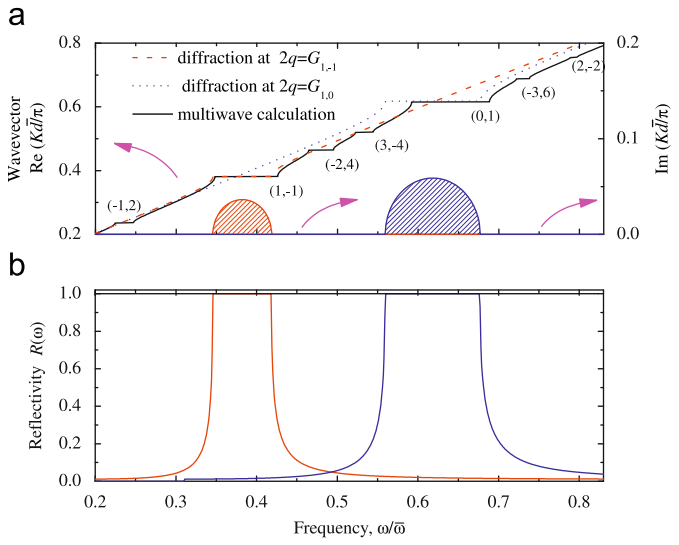

Fig. 15. (a) Extended-zone scheme of light dispersion in the Fibonacci chain of dielectric layers $\mathcal{A}$ and $\mathcal{B}$. Dashed and dotted curves are calculated in the two-wave approximation taking into account the mixing of the plane waves K and $K-G_{1,-1}$ or K and $K-G_{10}$, respectively. Curves bounding the shaded areas show the frequency dependence of the imaginary part of the light wave vector within the band gaps. Solid curve is calculated taking into account 12 terms in the sum (47). (b) The reflectivity $R(\omega)=|r|^2$ from the semi-infinite multilayered structure calculated in the two-wave approximation. The light frequency ω is related to the characteristic frequency $\bar{\omega}=\pi c/(\bar{d}\sqrt{\bar{\varepsilon}})$.

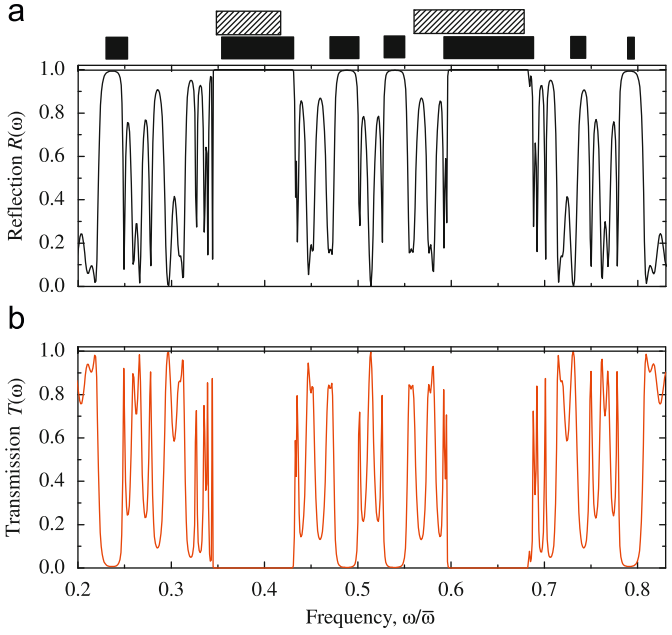

Fig. 16. The reflection (a) and transmission (b) spectra calculated for the finite Fibonacci sequence. The shaded and filled rectangles indicate the band gaps obtained in the two-wave approximation and the 12-wave calculation, respectively. The light frequency ω is related to the frequency $\bar{\omega}=\pi c/(\bar{d}\sqrt{\bar{\varepsilon}})$.

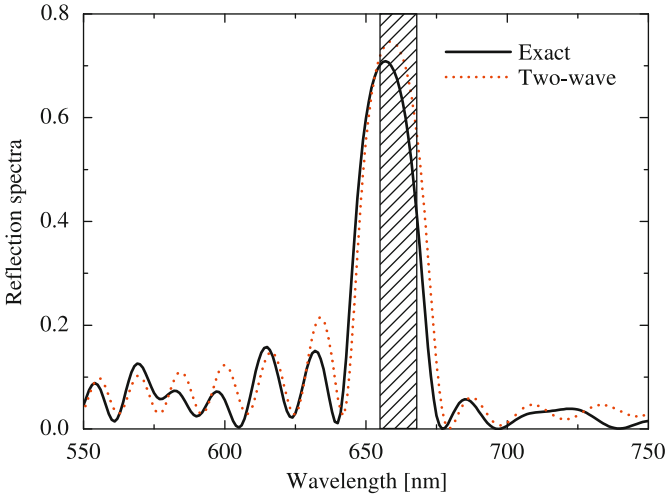

Fig. 17. Reflection spectra of Fibonacci quasicrystal studied in Ref. [8] and calculated exactly (solid line) and in two-wave approximation (dotted line). Shaded area corresponds to the stop-band region in infinite structure, analytically calculated in two-wave approximation. The values of parameters are indicated in text.

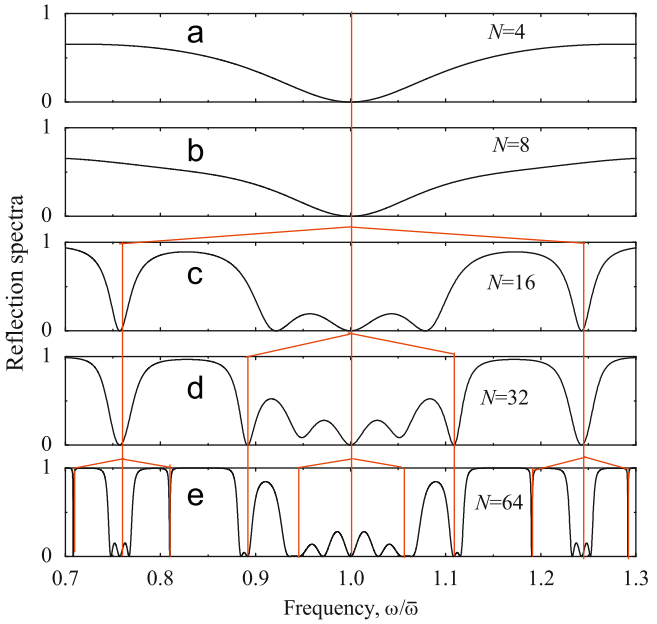

Fig. 18. Reflection spectra $R_N(\omega)$ of Thue–Morse chains containing $N = 4,\ldots, N = 64$ layers. Upturned-tree-like lines illustrate the multiplication of frequencies with zero reflectivity. The structure parameters are indicated in text.

12-wave calculation and shown by filled rectangles. The shaded rectangles correspond to the gaps found in the two-wave calculations taking into account the plane waves K, $K - G_{1,-1}$ either K, $K - G_{1,0}$.

Fig. 17 presents a comparison between the exact and approximate analytical reflection spectra from the Fibonacci quasicrystal. The structure consists of F_{10}=55 layers sandwiched between the air from left and semi-infinite substrate from right and arranged in the Fibonacci sequence $\mathcal{ABAABABA},\ldots$ (starting from the substrate). The parameters n_A=1.527, n_B=1.631, a = 139.7 nm, b=115.3 nm correspond to the system studied in Ref. [8] and schematically shown in Fig. 1. The value of substrate refractive index is taken as $n_{\rm subs}$=1.41. The structure is tuned to the Bragg condition (67) with $(h,h')=(0,1)$, $P_G=\omega\varepsilon_{G_{0,1}}/(2c\sqrt{\bar{\varepsilon}})$, and the wavelength corresponding to the stop-band center is $\lambda_G=2\pi c/(\omega_G)\approx 655$ nm. The exact spectra are calculated by using the transfer-matrix technique. Some details of this method are discussed in the Appendix. One can see from Fig. 17 that the two-wave approximation satisfactory describes the reflectivity peak inside the photoninc stop-band and the nearest interference fringes. Moreover, the figure demonstrates two effects due to presence of the interfaces structure-substrate and air-structure: (i) the interference fringes on the left and right sides of the stop-band are different, and (ii) the reflectivity-peak position is slightly shifted with respect to the center of the stop-band (the shaded area) in the infinite lattice. The both features are also reproduced by the two-wave approximation.

7. Thue–Morse structures: violation of the two-wave approximation

7.1. Trifurcations of optical spectra

The structure factor of a finite Thue–Morse lattice given by Eq. (38) mostly consists of non-Bragg peaks. In this section we demonstrate that the two-wave approach, discussed above and based on neglecting all except one diffraction vector in the structure factor, can be inappropriate to the description of this non-quasicrystal lattice.

Let us consider a Thue–Morse structure with parameters corresponding to SiN_x/SiO_2 multilayers studied in Ref. [74]: the refractive indices n_A = 2.23, n_B=1.45, and the layer thicknesses a and b satisfying the conditions $an_A=bn_B=\bar{\lambda}/4$, where $\bar{\lambda}=1.65\,\mu$m. Fig. 18 presents calculation of reflectivity spectra under normal light incidence for structures of different lengths sandwiched between two semi-infinite air layers. One can see that all the three have a pronounced dip centered at the frequency $\bar{\omega}=\pi c/(an_A+bn_B)=c(2\pi/\bar{\lambda})$. This result is clearly inconsistent with the two-wave approximation predicting a narrow stop-band at $\bar{\omega}$. Indeed, the structure factor (38) of the Thue–Morse chain has a Bragg peak at the wave vector $q=\pi/(a+b)$ with small but nonzero magnitude $|f(q)|\approx 0.11$. The origin of this peak is just the same as for the periodic Bragg mirror $(\mathcal{AB})(\mathcal{AB}),\ldots$. The phase shift of the wave passing through each period $(\mathcal{AB})$ forth and back equals 2π. Therefore the interference is constructive and leads to the Bragg diffraction. In the Thue–Morse structure $\mathcal{TM}_2=(\mathcal{AB})(\mathcal{BA})$ the order of layers in the second pair is interchanged, however, the optic path length for each pair remains the same as in the Bragg mirror, and one can expect the Bragg diffraction to survive. This conclusion is erroneous, as follows from the analysis of light reflection from two adjacent layers $\mathcal{B}$ surrounded by the layers $\mathcal{A}$,

$$r(\omega)=\frac{r_{BA}(1-e^{4iq_Bb})}{1-r_{BA}^2e^{4iq_Bb}}, \tag{69}$$

where r_{BA} = $(n_A - n_B)/(n_A + n_B)$ and $q_B=\omega n_B/c$. The factor $1-e^{4iq_Bb}$ vanishes at the frequency $\omega=\bar{\omega}$, where $q_Bb=\pi/2$. This destructive interference explains the central reflectivity dip for the structure $\mathcal{TM}_2=\mathcal{ABBA}$ shown in Fig. 18(a). Exactly the same argument leads to the reflectivity dip in the conjugated structure $\widetilde{\mathcal{TM}}_2=\mathcal{BAAB}$. Hence, the dip at the frequency $\omega=\bar{\omega}$ is also present in structures $\mathcal{TM}_3=\mathcal{TM}_2\widetilde{\mathcal{TM}}_2$, $\widetilde{\mathcal{TM}}_3=\widetilde{\mathcal{TM}}_2\mathcal{TM}_2$ as well as for all further generations $m\geq 2$. Thus, the Bragg diffraction described by Eqs. (39), (40) is suppressed due to the specific properties of structure geometry.

To proceed with the analysis of Fig. 18 we need other approaches more appropriate for the Thue–Morse structures.

One of them has been developed by Tamura and Nori in Ref. [60] where the transmission spectra of acoustic phonons through Thue–Morse superlattices is studied. Since the dispersion law of acoustic phonons are linear, the problem is formally similar to the photonic one. Tamura and Nori have demonstrated that the phonon transmission dips (corresponding to the reflectivity peaks) match the non-Bragg peaks of the structure factor. Another powerful approach is the transfer matrix trace-map technique. The transfer matrix $\hat{M}_m$ through the whole dielectric structure $\mathcal{TM}_m$ is given by a product of the transfer matrices $\hat{M}_A$, $\hat{M}_B$ through the layers of length a or b, respectively, lined up in accordance with the chain definition (15), (16). In the basis of electric field $E(z)$ and its derivative $-q^{-1}\ dE(z)/dz$ the transfer matrices are [75]

$$\hat{M}(qd)=\begin{pmatrix}\cos qd & -\sin qd\\ \sin qd & \cos qd\end{pmatrix}. \tag{70}$$

For non-absorptive dielectrics A and B, in which case the transfer matrices (70) are real, the transmission and reflection spectra, $T_m(\omega)$ and $R_m(\omega)$, are given by [75]

$$R_m(\omega)=1-T_m(\omega)=1-\frac{1}{x_m^2(\omega)+y_m^2(\omega)}, \tag{71}$$

where x_m and y_m stand for the half-trace $(M_{m,11}+M_{m,22})/2$ and half-antitrace $(M_{m,21}-M_{m,12})/2$ of the matrix $\hat{M}_m$, respectively. The half-traces x_m satisfy closed recurrence relations, also termed as trace maps [76]. For the Thue–Morse chains, the trace maps read

$$x_{m+1}=4x_{m-1}^2(x_m-1)+1. \tag{72}$$

In order to obtain optical spectra one also needs to consider the antitrace maps [77]

$$y_{m+1}=2x_{m-1}[(2x_m-1)y_{m-1}+\tilde{y}_{m-1}],$$

$$\tilde{y}_{m+1}=2x_{m-1}[(2x_m-1)\tilde{y}_{m-1}+y_{m-1}], \tag{73}$$

where the half-antitrace $\tilde{y}_m$ corresponds to the conjugated structure $\widetilde{\mathcal{TM}}_m$. Eqs. (72) and (73) allow one to derive the following property [59]:

$$\text{If } x_{m-2}(\omega)=0 \text{ then} \begin{cases} x_m(\omega)=x_{m+1}(\omega)=\cdots=1,\\ y_m(\omega)=y_{m+1}(\omega)=\cdots=0.\end{cases} \tag{74}$$

As a consequence, the transfer matrix $\hat{M}_m$ coincide with the unit 2×2 matrix $\hat{I}$ with the components $I_{j'j}=\delta_{j'j}$ $(j',j=1,2)$ and the structure becomes transparent at this frequency: $T_{m+k}(\omega)=1$, $R_{m+k}(\omega)=0$ $(k=0,1,2,\ldots)$. Whenever the half-trace $x_{m-2}(\omega)$ vanishes at some frequency $\omega=\omega_1$ and therefore, $x_m(\omega_1)=1$, there exist two neighboring frequencies, $\omega_2<\omega_1$ and $\omega_3>\omega_1$, such as $x_m(\omega_{2,3})=0$. According to Eq. (74), $x_{m+2}(\omega_{2,3})=1$, $y_{m+2}(\omega_{2,3})=0$ and the transmission coefficient for the structure $\mathcal{TM}_{m+2}$ at these frequencies reaches unity. Thus, the number of reflectivity dips increases with the structure order: each unitary peak in the spectrum of $\mathcal{TM}_m$ (i) persists in the spectra of the higher-order structures $\mathcal{TM}_{m+1},\mathcal{TM}_{m+2},\ldots$ and (ii) leads to appearance of two extra adjacent peaks for the structure $\mathcal{TM}_{m+2}$. Straight lines in Figs. 18(a)–(e) indicate this "tree" of trifurcations. The single reflectivity zero of the structure $\mathcal{TM}_2$ $(N=4)$ at $\omega=\overline{\omega}$ evolves into 11 zeroes of the structure $\mathcal{TM}_6$ $(N=64)$, cf. Figs. 18(a) and (e). The characteristic widths of the spectral features tend to zero proportional to a power $N_m^{-\gamma}=2^{-m\gamma}$ of the structure length, where γ is a frequency-dependent positive scaling index. Experimental observation of the frequency trifurcation in optical spectra of the Thue–Morse lattice has been reported in Ref. [78] for the SiO_2/TiO_2 dielectric structure. Note that the spectra also contain additional reflectivity dips, beyond the trifurcation tree, see, e.g., Fig. 18(c), however, generally they are not persistent with the structure order.

7.2. Lattice-like states

The spatial distribution of electric field at the frequencies with the unitary transmission has the so-called *lattice-like* shape, specific to the Thue–Morse structures [58]. These lattice-like states are illustrated in Fig. 19 for the generations $m=2,\ldots,6$ at the frequency $\omega=\overline{\omega}$. The spatial pattern of the electric field consists of two building blocks **A** (peak in $|E(z)^2|$) and **B** (dip in $|E(z)^2|$). Each block has the length $4\overline{d}$ and they are arranged in the Thue–Morse sequence. The field intensity profile for the chain $\mathcal{TM}_m$ forms the Thue–Morse chain $\mathbf{TM}_{m-2}$, composed of the blocks **A** and **B**.

The lattice-like spatial distribution is a direct consequence of the unitary transmission. At the frequency where $x_{m-2}=0$ one has $\hat{M}_m=\hat{\tilde{M}}_m=\hat{M}_{m+1}=\hat{\tilde{M}}_{m+1}=\cdots=\hat{I}$. Let us analyze the spatial distribution of electric field in the chain $\mathcal{TM}_{m+2}=\mathcal{TM}_m\widetilde{\mathcal{TM}}_m\widetilde{\mathcal{TM}}_m\mathcal{TM}_m$ with the length $4N_m=4\times 2^m$. The field profile in the last N_m layers is determined by the transfer matrix

$$\hat{M}_{m+2}^{(3N_m+k)}=\hat{M}_m^{(k)}\hat{\tilde{M}}_m\hat{\tilde{M}}_m\hat{M}_m=\hat{M}_m^{(k)}=\hat{M}_{m+2}^{(k)} \tag{75}$$

and matches that in the first N_m layers. Here the notation $\hat{M}_m^{(k)}$ stands for the transfer matrices through the first k layers of the chain $\mathcal{TM}_m$. Similarly, $\hat{M}_{m+2}^{(2N_m+k)}=\hat{M}_{m+2}^{(N_m+k)}$ so that the field in the layers $2N_m+1,\ldots,3N_m$ is the same as that in the layers $N_m+1,\ldots,2N_m$. This explains the **ABBA** profile of the field, where the blocks **A** and **B** stand for the field patterns in the structures $\mathcal{TM}_m$ and $\widetilde{\mathcal{TM}}_m$, respectively. Generalizing this result, we conclude that if $x_{m-2}(\overline{\omega})=0$ then the field at the frequency $\overline{\omega}$ in the structure $\mathcal{TM}_{m+l}$ is $\mathbf{TM}_l$-like. The length of blocks **A** and **B** constituting $\mathbf{TM}_l$ is 2^m.

Interestingly, perfect transmission peaks are also present in the so-called symmetrical Fibonacci photonic multilayers obtained by combining the Fibonacci sequence $\mathcal{F}_m$ with its mirror reflection, e.g., $(\mathcal{BA})(\mathcal{AB})$ for $m=3$. Such structures composed of

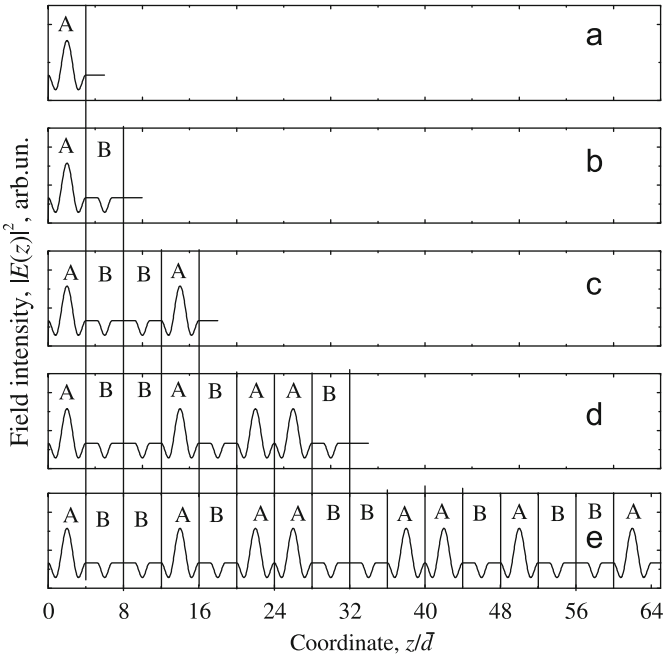

Fig. 19. Lattice-like distribution of the electric field in Thue–Morse chains containing $N_m=4,\ldots,64$ layers $(m=2,\ldots,6)$. Calculated at the frequency $\overline{\omega}=c\pi/(an_A+bn_B)$. Other parameters are the same as in Fig. 18.

alternating SiO_2 and negatively refracting layers were theoretically considered in Ref. [79]. Scaling behavior of optical transmission spectra has been found as well.

8. Photoluminescence of active aperiodic photonic structures

Control of spontaneous emission in periodic dielectric structures is being discussed since the pioneering papers by Bykov "Spontaneous emission in a periodic structure" [80] and Yablonovitch "Inhibited spontaneous emission in solid-state physics and electronics" [3] where photonic crystals were brought into focus of attention. For example, the modification of quantum-dot emission in 3D photonic crystals based on titania inverse opals has been reported in 2004 [81]. Not until recently such phenomena were addressed in deterministic aperiodic photonic structures. In this section we briefly consider the secondary light emission from active Thue–Morse [74] and Fibonacci [8] sequences and discuss effects of the pseudoband structure on emission properties of such systems. To simplify the analysis we take into consideration that the photoluminescence spectrum of a planar dielectric structure is proportional to its absorption spectrum calculated after adding a small imaginary part to the refractive indices of light-emitting layers. The rigorous proof of this result based on the Kirchhoff law of thermal radiation is given in Ref. [82].

8.1. Light-emitting Thue–Morse structures

Unusual spectral properties of the Thue–Morse chains open wide potential applications for the light emission control. Indeed, a lot of narrow resonances with a small reflectivity and a high transmission naturally appear in the optical spectra. These resonances allow the efficient light extraction from the structure at certain tunable frequencies. The first light-emitting Thue–Morse structure has been realized in Ref. [74]. Silicon-based materials SiN_x and SiO_2 are chosen for the $\mathcal{A}$ and $\mathcal{B}$ layers, respectively. Amorphous silicon nitride films have optically active defects producing a remarkable broadband light emission at room temperature [83]. On the other hand, SiN_x and SiO_2 are transparent in the visible range allowing the homogeneous optical pumping of complex multilayered samples.

The reflection spectra of Thue–Morse structures have already been discussed in Section 7. To illustrate the effect of Thue–Morse lattice on the light emission from the SiN_x layers we have calculated the absorbance $A(\omega)=1-R(\omega)-T(\omega)$. The small imaginary part $n_A''=10^{-4}$ is added to the refractive index of SiN layers. The absorption spectrum of 32-layered structure $\mathcal{TM}_5$ has a sharp maximum at the wavelength $\lambda^*\approx 1.19\,\mu$m where the reflection coefficient, in turn, has a dip. This wavelength lies within the wide featureless emission spectrum of the reference bulk SiN_x sample centered at $\lambda\sim 0.9\,\mu$m, see Fig. 20. The resonant enhancement of SiN_x room temperature photoluminescence at $\lambda=\lambda^*$ has been observed in Ref. [74]. This enhancement appears to be even more pronounced in the 64-layered structure where the absorption peak becomes sharper and the spatial distribution of the electric field attains the lattice-like shape. A possibility to use 2D generalization of Thue–Morse structures for engineering radiative rates and emission in photonic structures has been investigated theoretically in Ref. [84].

8.2. Active Fibonacci structures with embedded dye molecules

Photoluminescence modification of dye molecules embedded in a Fibonacci chain has been experimentally observed and theoretically

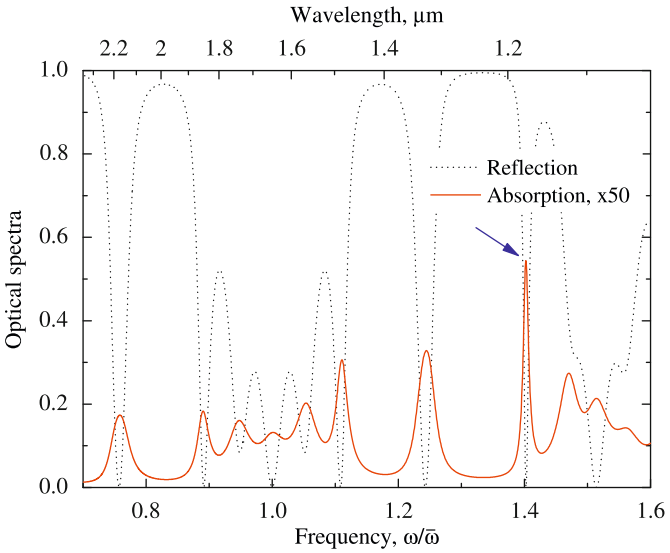

Fig. 20. Reflection and absorption spectra of a Thue–Morse chain containing $N=32$ layers. Calculated for n_A = 2.23 + i 10^{-4} and the same other parameters as in Fig. 18. The absorption spectrum is multiplied by a factor of 50 for better presentation. The inclined arrow indicates the absorption maximum at the wavelength $\lambda^*\approx 1.19\,\mu$m.

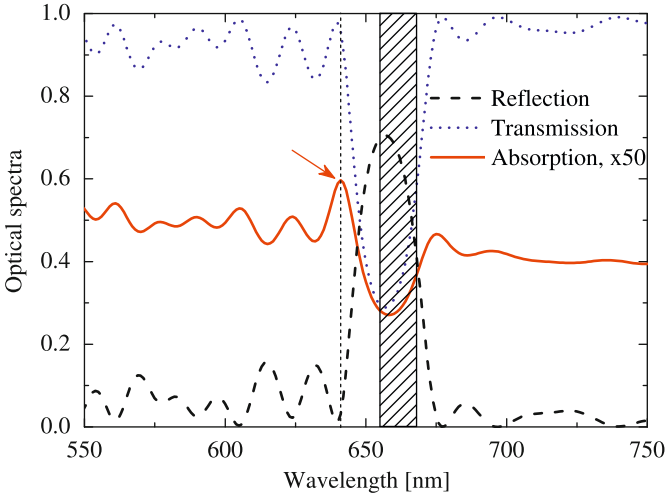

Fig. 21. Reflection, transmission and absorption spectra of Fibonacci quasicrystal studied in Ref. [8]. Absorption spectrum is multiplied by factor 50 for better presentation. Shaded area corresponds to the stop-band region in infinite structure, analytically calculated in two-wave approximation. Vertical line indicates the wavelength $\lambda^*\approx 640$ nm, absorption peak at this frequency is marked by inclined arrow. The values of parameters are given in text.

modelled by Passias et al. [8]. The structure under discussion is schematically shown in Fig. 1. Its parameters and reflection spectra are presented in Section 6.3: it consists of F_{10} = 55 layers of Cellulose Acetate (CA, layers $\mathcal{A}$) and Poly Vinyl Carbazole (PVK, layers $\mathcal{B}$) polymer materials grown on the glass substrate. The CA layers are infiltrated with the sulforhodamine dye. The dielectric contrast between different layers leads to the stop-band formation in the structure at the wavelength $\lambda_G\sim 655$ nm which, in turn, modifies the photoluminescence spectrum of dye molecules. To provide a qualitative insight into influence of the photon stop-band upon the dye emission we have plotted in Fig. 21 reflection, absorption and transmission spectra of the structure. The imaginary part $n_A''=10^{-4}$ was added to the refractive index of CA layers. The main features of the absorption spectrum shown in Fig. 21 are (i) suppression of absorption (and, therefore, emission) in the stop-band region, and,

(ii) absorption oscillations outside the stop-band region. Absorption peaks repeat maxima of the transmission spectrum since the light extraction from the more transparent structure is more effective. A very strong maximum corresponds to the wavelength $\lambda^* \sim 640$ nm (indicated by an arrow) where the spontaneous emission should be enhanced. Indeed, experimental measurements [8] reveal strong modulation of the photoluminescence spectrum in the photonic stop-band region with a sharp peak at the high-frequency band edge. Time-resolved measurements demonstrate a decrease in the photoluminescence decay lifetime from 4.4 ns (off-resonance wavelength) to 3.9 ns (on-resonance wavelength). This modification of emission spectra is similar to that in periodic photonic crystals [85] and related to interference fringes near the photonic (pseudo)band gap. However, it should be emphasized that, in Ref. [8], the effect has been observed in *nonperiodic* quasicrystalline photonic structure.

9. Resonant aperiodic photonic structures

Periodic structures in which the dielectric response of at least one composite materials as a function of frequency ω has a pole at a resonance frequency are grouped into a specific class of resonant photonic crystals whose normal waves are polaritons. Similarly one can define resonant photonic quasicrystals and other aperiodic deterministic sequences. This section concerns their optical spectroscopy near the exciton and plasmon resonant frequencies.

9.1. Exciton–polaritonic Fibonacci quantum-well structures

If the light frequency lies in the vicinity of the exciton resonant frequency then, in general, a photon and an exciton mix and form a combined quasi-excitation called the exciton polariton. De Medeiros et al. [86] were the first who theoretically investigated the propagation of exciton–polaritons in quasiperiodic binary superlattices of Fibonacci type. The layer A was represented by a spatially dispersive medium modelled by a semiconductor from the nitride family (GaN) which alternated with a typical dielectric medium B (sapphire). The taken layer thicknesses were $a = b =$ 500 Å which means that the exciton Bohr radius was small as compared with a. Therefore, the exciton can be considered as a bulk-like particle in the same way as it is treated in thin films [87] and optical superlattices [88]. The distribution of the allowed and forbidden energy bandwidths of the exciton polaritons is calculated in Ref. [86] for the periodic approximants as a function of the Fibonacci generation index m. Scaling and localization of exciton polariton modes propagating in these quasiperiodic structures are also described. As m increases, the allowed band regions get narrower and narrower, as an indication of greater localization of the exciton–polariton modes, characterizing a Cantor-like spectrum.

In Ref. [46] a new kind of resonant photonic quasicrystals has been proposed, namely, a multiple QW-structure with the exciton resonant frequency tuned to the resonant Bragg condition (58). The allowed diffraction vectors $G_{hh'}$ form a dense pseudocontinuous set. According to Eq. (27) the largest values of $|f_{hh'}|$ are reached for the diffraction vectors $G_{hh'}$ with pairs h, h' coinciding with two successive Fibonacci numbers F_m, F_{m-1}. Thus, for $(h, h') = (F_m, F_{m-1}) = (1,0), (1,1), (2,1), (3,2)$ and (5,3) corresponding to $m = 1,\ldots,5$, the modulus of $f_{hh'}$ equals to $\approx$ 0.70, 0.88, 0.95, 0.98 and 0.99, respectively. It follows then that if the exciton resonance frequency satisfies the condition

$$\frac{\omega_0 n_b}{c}\overline{d} = \pi\left(F_m + \frac{F_{m-1}}{\tau}\right), \quad m = 1,2,\ldots \tag{76}$$

one can expect the structure to show superradiative behavior, similarly to the superradiance of a periodic multiple quantum-well structure with the period d tuned to the resonance condition [45]

$$\frac{\omega_0 n_b}{c} d = \pi. \tag{77}$$

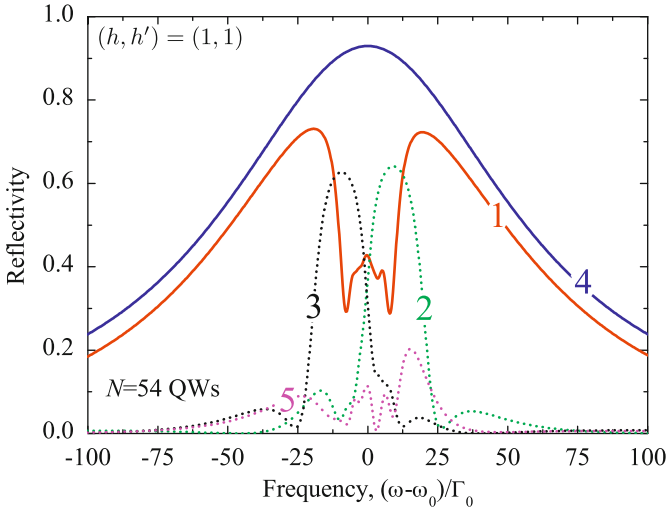

Fig. 22. Reflection spectra calculated for three Fibonacci structures satisfying the resonant Bragg condition (76) for $m = 2$ (curve 1) and detuned by $\pm 2\%$ from this condition (curves 2 and 3) in comparison with the reflection spectrum from the periodic resonant Bragg QW structure (curve 4) and weakly disordered periodic structure (curve 5). The values of parameters are indicated in the text.

Fig. 22 presents reflection spectra calculated for four structures containing N=54 quantum wells. The exciton parameters used are as follows: $\hbar\omega_0 = 1.533$ eV, $\hbar\Gamma_0 = 50$ μeV, $\hbar\Gamma = 100$ μeV, $n_b =$ 3.55. Curve 1 is calculated for the resonant canonic Fibonacci QW structure satisfying the exact Bragg condition (76) with m=2. Curves 2 and 3 correspond to the Fibonacci structures also with $a/b = \tau$ but the barrier thicknesses slightly detuned so that the average period differs from the exactly tuned period by a factor of 1.02 for curve 2 and 0.98 for curve 3. Curve 4 describes the reflection from the periodic Bragg structure with the same exciton parameters and the period $d = \pi/q(\omega_0)$, satisfying Eq. (77). Curve 5 presents for comparison reflection spectrum from weakly disordered periodic structure, where QW coordinates are given by Eq. (28) with $\overline{d} = \pi/q(\omega_0)$ and $\sigma_z = \overline{d}/4$. From comparison of curves 1 and 4 we conclude that the reflection spectra from the resonant Fibonacci and periodic structures tuned to the Bragg conditions (76) and (77) are close to each other outside the frequency region around ω_0. Moreover it follows from curves 2 and 3 that a slight deviation from the condition (76) results in a radical decrease of the effective spectral halfwidth. Thus, the sensitivity to the resonance condition, the characteristic of periodic Bragg QW systems, holds also for aperiodic QW systems like the Fibonacci structures. The remarkable structured dip in the middle of the spectrum 1 is the only qualitative difference from the periodic structures, this dip is a consequence of an allowed exciton–polariton band lying between the frequencies $\omega_{\rm in}^{\pm}$ defined in Eq. (60). We remind that for a periodic resonant Bragg structure an inner allowed band is absent, $\omega_{\rm in}^{+} = \omega_{\rm in}^{-}$. Now we turn to analysis of reflection spectra as a function of the QW number N and index j in Eq. (76).

Evolution of the reflection spectra with the QW number is illustrated in Fig. 23. The spectral envelope shows a behavior similar to that of the conventional Bragg QW structure. Indeed, for small N the envelope is a Lorentzian with the halfwidth increasing as a linear function of N. This is a straightforward manifestation of superradiant regime, which, as one can see here, does not necessarily require periodicity even if the inter-well distances

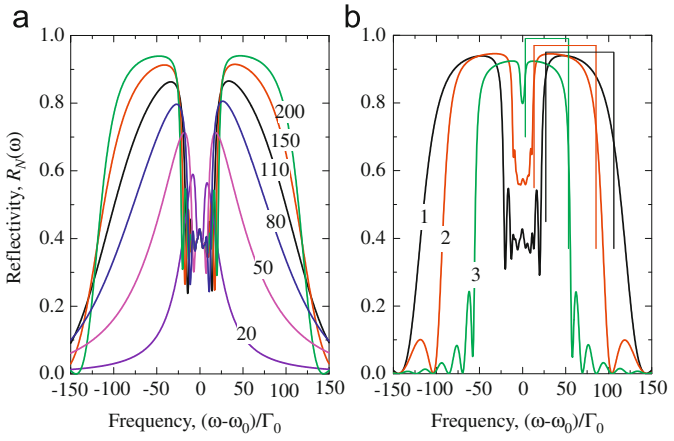

Fig. 23. Reflection spectra from the resonant Fibonacci structures. (a) Six curves are calculated for the structures satisfying the condition (76) with m = 2 and N = 20, 50, 80, 110, 150, 200. The number of wells is indicated near each corresponding curve. (b) Curves 1, 2, 3 are calculated for the structures with N = 200 and indices m = 2, 3, 5 in Eq. (76). Vertical lines connected by a horizontal bar indicate the exciton–polariton high-frequency gap given by Eq. (60). Other parameters are the same as in Fig. 22.

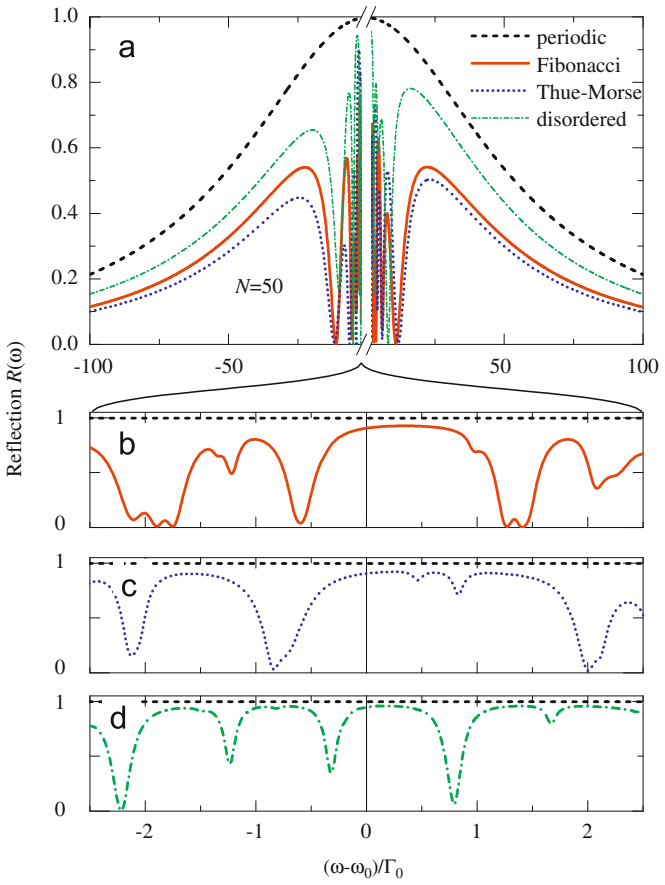

Fig. 24. Reflection spectra calculated for four QW structures, each containing 50 wells and tuned to the resonant Bragg condition $2\bar{d}=\lambda(\omega_0)$: periodic structure, with $a\equiv b\equiv\bar{d}$ (dashed); Fibonacci chain, with $a/b=\tau$ (solid curve); Thue–Morse sequence with a/b = 3/2 (dotted); and weakly disordered periodic MQWs, see Eq. (29), with $\sigma_z=\lambda_0/20$ (dashed-and-dotted). Note the break on the abscissa axis in panel (a) around $\omega=\omega_0$. Panels (b)–(d) show the same spectra in larger scale of the variable $(\omega-\omega_0)/\Gamma_0$. Calculated for $\hbar\Gamma_0=50\,\mu$eV, $\hbar\omega_0=1.533$ eV, $\Gamma=0.1\Gamma_0$. From Ref. [89].

are comparable to the light wavelength. The saturation of the spectral halfwidth (photonic crystal regime) begins at large N of the order of $\sqrt{\omega_0/\Gamma_0}$, in a similar way as for the periodic Bragg structures. The shape of the spectra for large N confirms existence of two wide symmetrical stop bands in the energy spectrum of the structure with an allowed band between them, as described by Eq. (60). Of course, the terms "allowed" and "stop" bands to an aperiodic structure are applicable in a reasonable sense assuming the two-wave approximation.

Fig. 23(b) presents the reflection spectra of Fibonacci QW structures containing a large number of wells, N = 200, and satisfying Eq. (76) for three different values of m. All the curves indicate an existence of allowed and stop bands, in accordance with Eq. (60).

Fig. 24 presents the reflectivity $R_N(\omega)$ calculated for the light normally incident from the left half-space $z<0$ upon four different 50-QW structures. All the four, namely, the Fibonacci, Thue–Morse, periodic and distorted periodic structures, are tuned to satisfy the Bragg resonant condition (76) which can be rewritten as $\lambda(\omega_0)=2\bar{d}$, where $\lambda(\omega)=2\pi c/(\omega n_b)$. This means that, for the Fibonacci structure, the value G of diffraction vector is set to $G_{hh'}$ with $h=1, h'=0$ and, therefore, for the four structures $G=2\pi/\bar{d}$ and they have approximately the same length $L=N\bar{d}$ and are different only by details of the QW arrangement. Therefore, their optical properties can be conveniently compared.

One can see from Fig. 24 that the resonant Bragg condition leads to high reflectivity of not only the periodic and quasicrystalline Fibonacci chains but also the Thue–Morse and slightly disordered periodic structures. In the region $|\omega-\omega_0|>20\Gamma_0$, far enough from the exciton resonance frequency, the four spectra have similar Lorentzian wings with the halfwidth of the order of $N\Gamma_0$ indicating the existence of a superradiant exciton–polariton mode. The magnitude of the wings is governed by a modulus of the structure-factor coefficient, $|f_G|$. For the chosen structures this value runs from $|f_G|=1$ (periodic structure) and $|f_G|=0.95$ (distorted periodic) to $|f_G|=0.70$ (Fibonacci) and $|f_G|=0.65$ (Thue–Morse). The spectral wings in Fig. 24 decline monotonously with decreasing $|f_G|$. In addition it should be mentioned that, for the Fibonacci QW structure tuned to $G_{hh'}$ with $h=1, h'=1$, see Fig. 22, the structure-factor coefficient is $|f_G|\approx 0.9$ and the spectral wings in reflectivity are raised as compared with those for the Fibonacci structure tuned to $G_{1,0}$.

In the frequency region around ω_0 the reflection spectra from the nonperiodic structures show wide dips where the reflection coefficient oscillates with the period of oscillations decreasing as ω approaches ω_0. The spectral dip naturally appears for a multilayered deterministic system tuned to a Bragg diffraction vector with the structure-factor coefficient f_G smaller than unity, and it widens as the value of $1-|f_G|$ increases. Thus, Fig. 24(a) demonstrates that in the wide spectral range the reflectivity spectrum of the Bragg MQW chain depends only on three geometrical parameters: QW number N, Bragg diffraction vector G and structure factor f_G.

Further geometry-related peculiar spectral properties are revealed in the narrow resonance region around ω_0 ranged over few values of Γ_0, see Figs. 24(b)–(d). In realistic semiconductor QWs the nonradiative decay rate is larger than or comparable to Γ_0, and the majority of spectral fine-structure features are smoothed [9]. For small nonradiative damping rates Γ (lying beyond experimentally available values), an intricate fine structure of optical spectra is developed in this region. All the considered aperiodic structures possess a narrow middle stop-band embracing the exciton resonance ω_0. In particular, for the Fibonacci QW structure this stop-band is located between $\omega_0-0.4\Gamma_0$ and $\omega_0+0.9\Gamma_0$. The spectral properties in the frequency range $|\omega-\omega_0|\sim\Gamma_0$ for $\Gamma\ll\Gamma_0$ are discussed in Section 9.2 in more details.

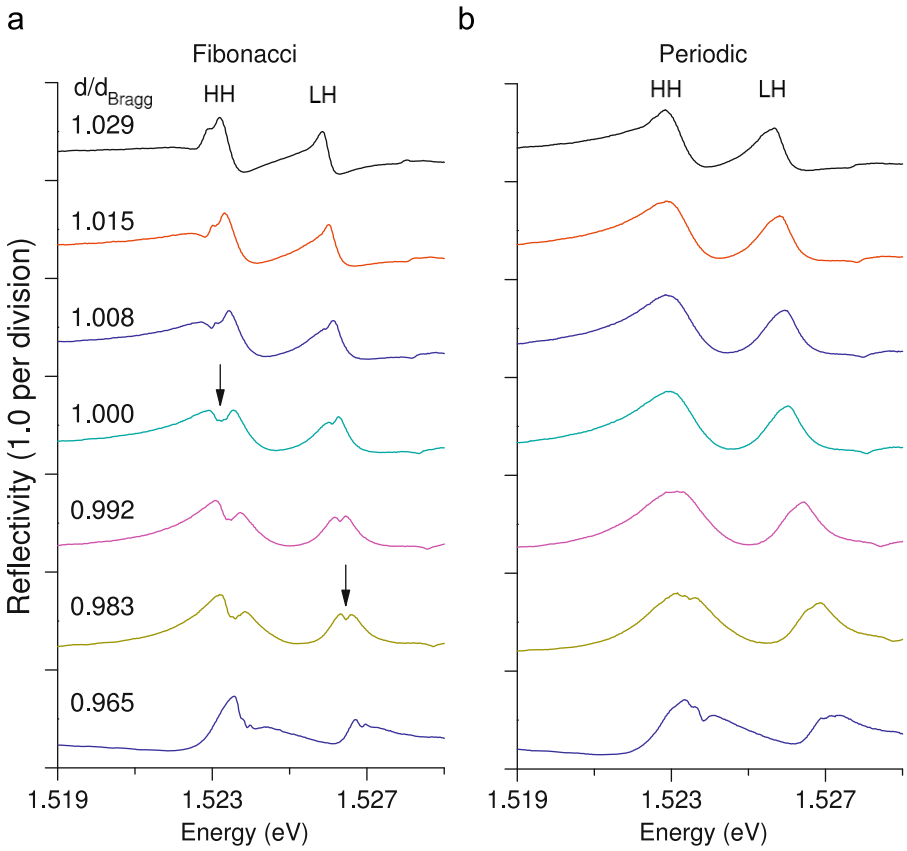

Fig. 25. Comparison of the thickness dependence of the reflectivity. The spacing of 21 QWs is either (a) a Fibonacci sequence with optical thicknesses of $b=0.36\lambda(\omega_0)$ and $a=0.59\lambda(\omega_0)$ or (b) equidistant at $\lambda(\omega_0)/2$. A reflectivity dip is present at the Bragg resonance only in (a). Curves are labelled by the ratio d/d_{Bragg}, where $d_{\mathrm{Bragg}}=\lambda(\omega_0)/2$, $\lambda(\omega_0)$ is the wavelength of the light inside the sample at the exciton resonance frequency, d is the average interwell distance. Each curve of larger d/d_{Bragg} is shifted up by one unit of reflectivity from the preceding one. From Ref. [9].

Fig. 25 compares the measured reflectivity for two graded samples with N = 21: (a) Fibonacci QW sequence and (b) periodically spaced MQWs [9]. A reflectivity maximum with broad linewidth occurs at the Bragg condition in both samples for both the heavy-hole (HH) and the light-hole (LH) resonances. This maximum is just the well known photonic stopband, which is in agreement with previous work on 1D resonant photonic crystals. Notably, however, the stop band is smooth for the crystalline structure, whereas it reveals a pronounced fine structure (dips, see arrows) for the Fibonacci quasicrystals. This fine structure is visible for both the heavy- and the light-hole exciton resonances, strongly suggesting that this signature is a fingerprint of the quasicrystal, see Fig. 22.

Fig. 26 presents the calculated and the measured reflection for the 54 Fibonacci-spaced quantum wells. Due to the Fibonacci spacing, the spectrum displays multiple features which all are very well reproduced by the theory [10]. In order to take explicitly into account the disorder in the experimentally realized samples the exciton nonradiative damping rate is assumed to be frequency-dependent as follows:

$$\Gamma(\omega)=\frac{\Gamma}{1+\exp[-\hbar(\omega-\omega_0+\Omega_{\mathrm{cut}})/C]}.$$

For the heavy-hole resonance, the best fit is obtained for the following set of constants: 0.163 meV for $\hbar\Gamma$, 0.25 meV for the cut-off energy $\hbar\Omega_{\mathrm{cut}}$ and 0.1 meV for C. The refractive indices of the layers are fitted using a single small set of parameters such

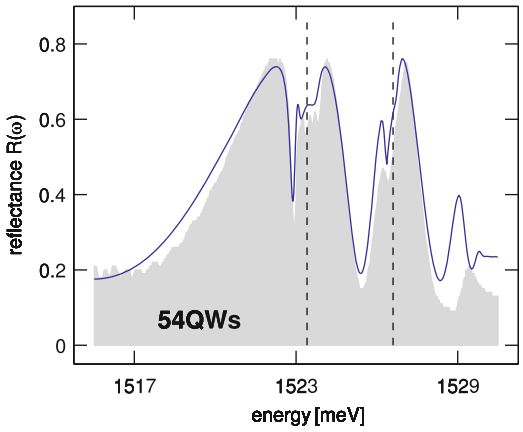

Fig. 26. Fit (solid curve) to measured reflection spectrum (shaded area) for 54 Fibonacci-spaced QWs using a frequency-dependent dephasing $\Gamma(\omega)$. From Ref. [10].

that the calculations reproduce both the single-QW and 54-QW measured reflection spectra.

9.2. *Scaling and self-similarity in the optical spectra of Fibonacci QW structures*

Now we concentrate on the narrow frequency region $|\omega-\omega_0|\sim\Gamma_0$ and neglect the nonradiative decay of excitonic polaritons, assuming $\Gamma=0$. In this regime the optical spectra and the exciton–polariton dispersion are very intricate, demonstrating

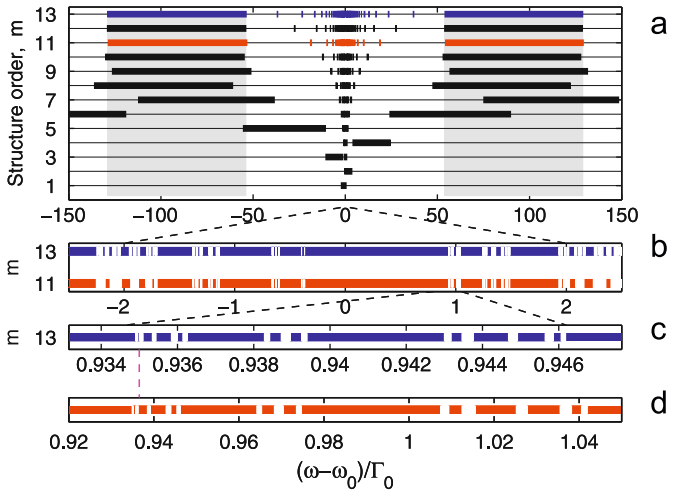

Fig. 27. (a) Exciton–polariton allowed (thin lines) and forbidden (thick stripes) bands in periodically repeated Fibonacci sequences of the order m = 1, …, 13. (b) Bands for m = 11 and 13 in the spectral range around the frequency $\omega=\omega_0$. (c), (d) Bands for m = 11 and 13 in larger scales near the frequency $\omega=\omega_0+0.935\Gamma_0$ indicated by the vertical dashed line. Calculated for $(h,h')=(1,0)$, $\hbar\Gamma_0=50\,\mu$eV, $\hbar\omega_0=1.533$ eV and zero exciton nonradiative decay, $\Gamma=0$. From Ref. [89].

scaling invariance and self-similarity [89]. In order to reveal the behavior of exciton polaritons it is instructive to calculate the polariton dispersion in the approximants [39] of the aperiodic chains containing the periodically repeating sequences $\mathcal{F}_m$. In such periodic systems the polariton band structure consists of allowed minibands and forbidden gaps. The gaps are found from the condition [90]

$$|x_m(\omega)|>1, \tag{78}$$

where x_m is the half-trace $(M_{11}+M_{22})/2$ of the structure transfer matrix $\hat{M}$. Hereafter we use the notation $\mathcal{F}_m$ for the Fibonacci chain containing $N=F_m$ QWs starting from the trivial chain $\mathcal{F}_1$ that consists of one segment $\mathcal{A}$. The transfer matrix $\hat{M}_m$ through the whole structure $\mathcal{F}_m$ is given by a product of the transfer matrices $\hat{M}_{QW}$ through a QW and transfer matrices $\hat{M}_A$, $\hat{M}_B$ through the barrier of length a or b, respectively, taken in the Fibonacci sequence. The barrier transfer matrices are given by Eq. (70). In the basis of electric field $E(z)$ and its derivative $-q^{-1}dE(z)/dz$, the QW transfer matrix has the form [90]

$$M_{QW}=\begin{pmatrix}1 & 0\\ 2S & 1\end{pmatrix},\quad S=\frac{\Gamma_0}{\omega_0-\omega}. \tag{79}$$

For the Fibonacci chains, the half-traces satisfy trace maps [76]

$$x_{m+1}=2x_mx_{m-1}-x_{m-2}. \tag{80}$$

The polariton energy spectrum is determined by the general properties of nonlinear transformations (80) and the initial conditions specific for the QW transfer matrices (79). The trace maps are an efficient tool in studies of the spectral properties of deterministic aperiodic structures [91,48]. The band calculations are presented in Fig. 27(a), where the black stripes and horizontal lines show, respectively, the forbidden and allowed bands for different values of the structure order m ranging from m=1 to 13. Figs. 27(b)–(d) represent this band sequence for m=11 and 13 in different frequency scales. Panel (a) demonstrates that two broad band gaps are already present for 21 QWs (m=8). With increasing m their edges very quickly converge to the analytical values from Eq. (60) shown by the gray rectangles in Fig. 27(a). A narrow permanent middle band gap at $-0.4\Gamma_0\lesssim\omega-\omega_0\lesssim0.9\Gamma_0$ is well resolved in the frequency range of Fig. 27(b).

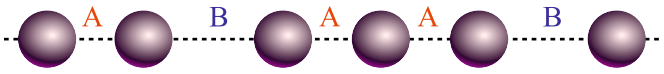

Fig. 28. One-dimensional quasiperiodic array of metal nanoparticles with the Fibonacci sequence of distances a and b between adjacent particles: $a,b,a,a,b,\ldots$.

The other forbidden bands depicted in Fig. 27 can be interpreted in terms of two formation mechanisms. The first mechanism is related to the two-wave approximation. In this approximation the half-trace of the transfer matrix x_m reaches minimum (-1) or maximum $(+1)$ values at particular frequencies ω_s where the reflectivity r_N, given by Eq. (66), vanishes. Using Eq. (66) one can check that at these frequencies the product QNd is an integer number of π. Let $x_m^{(2\text{-wave})}$ be the half-trace calculated in the two-wave approximation. In the vicinity of ω_s its frequency dependence can be described by $x_m^{(2\text{-wave})}(\omega)=n_s[1-u_s(\omega-\omega_s)^2]$, where $n_s=\pm1$ and u_s is a positive coefficient. Near ω_s the exact function $x_m(\omega)\equiv\mathrm{Tr}(\hat{M}_m)/2$ differs from $x_m^{(2\text{-wave})}(\omega)$ by the correction $\delta x(\omega)$ which can be approximated by $n_s[c_s+v_s(\omega-\omega_s)]$ where c_s, v_s are additional constants. As a result the behavior of the half-trace can be presented in the form

$$x(\omega)=n_s\left[1+c_s+\frac{v_s^2}{4u_s}-u_s\left(\omega-\omega_s-\frac{v_s}{2u_s}\right)^2\right].$$

If $c_s+(v_s^2/4u_s)$ is positive then the periodic system has a gap at $\omega_s'=\omega_s+(v_s/2u_s)$.

The second mechanism of gap formation is related to localized exciton–polariton states rather than to the Fabry–Pérot interference and can be treated in terms of self-similarity effects. Particularly, in the frequency range $|\omega-\omega_0|\sim\Gamma_0$ the number of stop-bands increases while their widths tend to zero as $N\to\infty$. As a result, the sequence of the allowed and forbidden bands becomes quite intricate, see Figs. 27(b)–(d), and locally resembles the Cantor set [92]. The most striking result in Fig. 27(b) is similarity of the band structure of the approximants with m = 11 and 13. On the other hand, the spectrum for m = 13 has a lot of narrow band gaps not resolved in the scale of Fig. 27(b). Figs. 27(c) and (d) present the same spectra in larger scales near the right edge of the middle band gap, with the scale for m = 13 being $\lambda_+\approx8$ times larger than that for m = 11. Matching the bandgap positions we prove the existence of the spectral scaling in the Fibonacci QW structures. The scaling index λ_+ specifies the ratio of the widths of spectral features of the structures with the order differing by two. The scaling properties hold not only for the band positions but for the whole curves $x_m(\omega)$ and are manifested in transmission spectra as well. This self-similarity of band structure of Fibonacci sequences with the orders m differing by 2 can be related to the so-called "band-edge" cycle of the trace map (80) [93,89].

The polariton band-structure calculations performed for Thue–Morse QW structures lead to qualitatively similar conclusions: two-wave band gaps are already formed for small m, a middle narrow band gap is always present, and a complicated sequence of the allowed and forbidden bands arises around ω_0 [89]. These spectral features can be interpreted in terms of zero reflection frequencies, similarly to Fig. 18.

9.3. Aperiodic arrays of metallic spheres

Aperiodic arrays of ellipsoidal metal nanoparticles are considered in Refs. [94–96,32]. Fig. 28 illustrates a linear Fibonacci chain of metallic spheres. In order to describe the plasmon modes in the quasiclassic point-dipole approximation, one needs to solve

the Maxwell equation

$$\mathrm{div}\,\boldsymbol{D}(\boldsymbol{r},\omega)=0,\quad \boldsymbol{D}(\boldsymbol{r},\omega)=\boldsymbol{E}(\boldsymbol{r},\omega)+4\pi\boldsymbol{P}(\boldsymbol{r},\omega),$$

$$4\pi\boldsymbol{P}(\boldsymbol{r},\omega)=4\pi\sum_j \boldsymbol{p}_j\delta(\boldsymbol{r}-\boldsymbol{r}_j)=\boldsymbol{E}(\boldsymbol{r},\omega)+V_0[\varepsilon(\omega)-1]\sum_j \boldsymbol{E}(\boldsymbol{r}_j,\omega)\delta(z-z_j)\delta(x)\delta(y),$$

where $\boldsymbol{E}(\boldsymbol{r},\omega)$ is the electric field, $\boldsymbol{p}_j$ is electric-dipole moment of the j-th particle, $\boldsymbol{r}_j=(0,0,z_j)$, z_j is the z-coordinate of the j-th particle, and

$$\varepsilon(\omega)=1-\frac{\omega_p^2}{\omega(\omega-\mathrm{i}\gamma)}.$$

This approximation is valid as long as the interparticle separation is much smaller compared with the wavelength of the electromagnetic field. The plasma frequency of a spherical metal particle, $\omega_{p,\mathrm{sph}}$, is related to that of the bulk metal, ω_p, by $\omega_{p,\mathrm{sph}}=\omega_p/\sqrt{3}$. The eigenfrequencies of dipolar modes can be presented in the form

$$\Omega_m=\omega_p\sqrt{\frac{1}{3}-\frac{1}{4}\left(\frac{\gamma}{\omega_p}\right)^2+U\beta_m},$$

where U is a constant, m is the modal index and β_m are eigenvalues of the matrix $\boldsymbol{Q}$ defined by

$$Q_{ij}=\begin{cases}0 & \text{for } i=j,\\ \dfrac{a^3}{|z_i-z_j|^3} & \text{for } i\neq j.\end{cases}$$

In Ref. [95] eigenvalues of β are arranged in the increasing order $\beta_1\le\beta_2\le\cdots\le\beta_m\cdots\le\beta_N$. Fig. 29(a) shows the dependence of β on the normalized modal index $s\equiv(100/145)m$ for a system with N=145. For large number N of nanoparticles the electric field $\boldsymbol{E}(z)$ at x = 0, y = 0 corresponding to particular value of m can be expanded in terms of the exponential functions $\exp[\mathrm{i}(K_m-G_{hh'})z]$ with $K_m=\pi m/L$, where m = 1,2,…,N and L is the Fibonacci chain length $N\bar{d}$. The normalized modal index is expressed via K_m as $s=100(K_m\bar{d}/\pi)$. For a periodic array, a = b, the dispersion $\beta(s)$ ($1\le s\le 100$) or Ω_m ($1\le m\le 145$) is a smooth monotonic function, see black diamonds in Fig. 29(a) and solid curve in Fig. 29(b). For the differing lengths a and b, the dependence $\beta(s)$ or Ω_m exhibits plasmonic gaps at K satisfying the condition $K=G_{hh'}/2=(\pi/\bar{d})(h+h'/\tau)$. In terms of s and m this condition is rewritten as

$$s=100\left(h+\frac{h'}{\tau}\right),\quad m=145\left(h+\frac{h'}{\tau}\right).$$

In particular, in Figs. 29(a) and (b) the gaps are related to the pairs $(h,h')=(2,-3)$, $(-1,2)$, $(1,-1)$, $(0,1)$, $(2,-2)$, $(-1,3)$, etc.

For $b/a\gg 1$, the system is decomposed into clusters containing two or three particles and, in addition, one particle for the Fibonacci sequences with odd generation indices. The eigenvalues β of two interacting nanoparticles are $\beta_1^{(2)}=-1$ and $\beta_1^{(2)}=+1$; the eigenvalues β of three equally spaced nanoparticles are $\beta_1^{(3)}=(1-3\sqrt{57})/16$, $\beta_2^{(3)}=-0.25$ and $\beta_3^{(3)}=(1-3\sqrt{57})/16$, and the eigenvalue β for a single isolated particle is equal to zero. One can see from Fig. 29 that with increasing ratio b/a the eigenvalues of β are gathering around five values, $\beta_l^{(2)}(l=1,2)$ and $\beta_l^{(3)}(l=1,2,3)$. The number of degeneracy at $b/a\to\infty$ is equal to the number of corresponding clusters in the chain, 23 for $\beta=\pm 1$ and 33 for $\beta=\beta_l^{(3)}$. These studies have been extended to ferromagnetic nanoparticles in Ref. [96]. The 2D quasicrystalline array of metallic nanoparticles has been theoretically studied in Ref. [97]. A rich variety of plasmonic modes has been found with very different spatial localization characteristics and radiative decay rates. Experimental realization of 2D lithographically defined deterministic aperiodic arrays of gold nanoparticles is reported in Ref. [32]. Spatially averaged enhancement of Raman scattering by the factor $\sim$107 has been observed.

10. Two- and three-dimensional photonic quasicrystals

10.1. Penrose lattice and related quasicrystals

The Penrose tiling is one of the most famous and charming quasicrystalline lattices. Indeed, the pioneering paper by Penrose [98] is even entitled as "The Role of Aesthetics in Pure and Applied Mathematical Research". There are many different kinds of the Penrose tilings. The common feature of all of them, termed as *decagonal phase* [99] is a 10-fold orientational symmetry of the diffraction images. The canonic Penrose tiling [99] is shown in Fig. 30(a), it consists of rhombuses of two kinds with acute angle equal to either $2\pi/10$ or $2\pi/5$. Its 2D Fourier image is presented in Fig. 30(b).

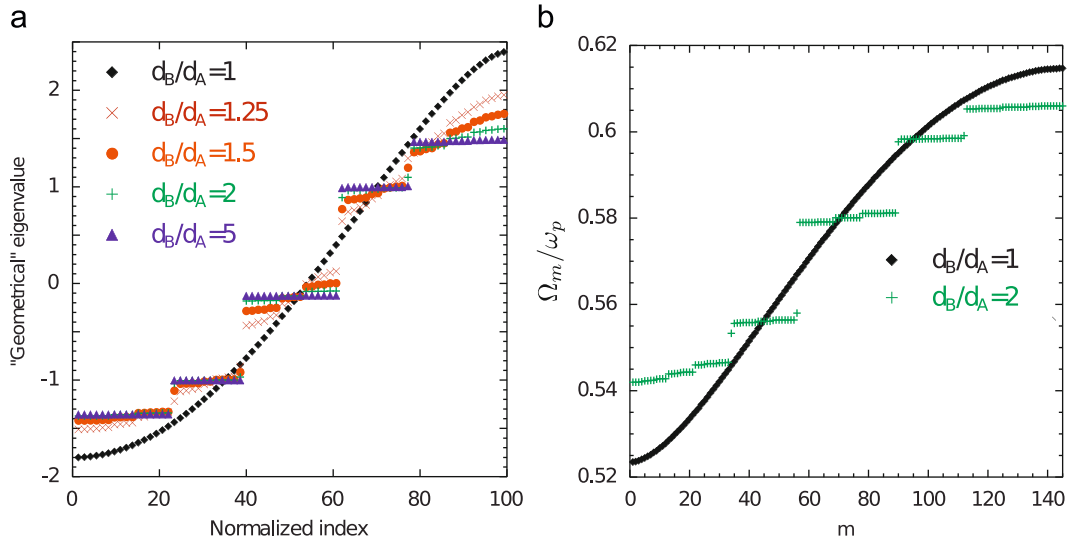

Fig. 29. Linear Fibonacci chain with the generation index j = 10. (a) "Geometrical" eigenvalues β versus the modal index normalized to 100% for b/a = 1 (♦), b/a = 1.25 (×), b/a = 1.5 (•), b/a = 2.0 (+), and b/a = 5.0 (▲). (b) Eigenfrequency of the longitudinal mode versus the modal index m. After Ref. [95].

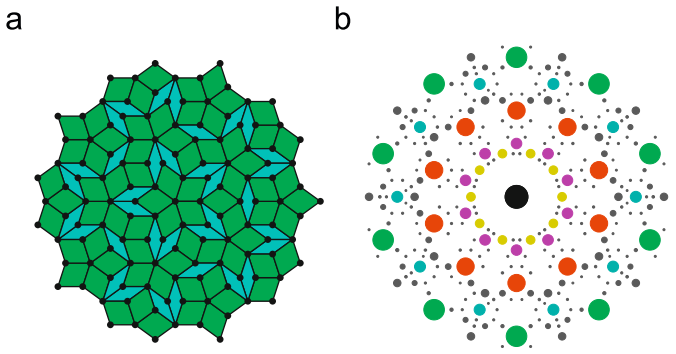

Fig. 30. (a) Canonic Penrose tiling. (b) Calculated diffraction image of this tiling. The diameter of each spot located at the point $\boldsymbol{G}$ is proportional to the absolute value of the structure factor $|f_{\boldsymbol{G}}|$, where $\boldsymbol{G}$ is the Bragg diffraction vector (86).

Three equivalent ways to define Penrose tiling include (i) matching rules for the arrangement of thick and thin rhombuses [100–102], (ii) the cut-and-project scheme from a periodic lattice in the five-dimensional hyperspace, [103] and (iii) dual multigrid techniques [104]. In this section we briefly review the last approach, namely, the generalized dual multigrid technique. Its advantage is a possibility to generate quasicrystalline lattices with arbitrary rotational symmetry. The dual multigrid technique consists of the two basic steps: (i) generation of the grid with desired rotational symmetry and (ii) dual transformation from the grid to the quasicrystalline lattice. To construct the grid corresponding to the Penrose tiling, we define five basic vectors $\boldsymbol{e}_n$ forming a regular star

$$\boldsymbol{e}_n = \left[\cos\left(\frac{2\pi n}{5}\right), \sin\left(\frac{2\pi n}{5}\right)\right], \quad n = 0, \ldots, 4. \tag{81}$$

Then we introduce five sets of the parallel lines $\boldsymbol{r}_n$ each set normal to the corresponding star vector

$$\boldsymbol{r}_{n,j} \cdot \boldsymbol{e}_n = x_n(j), \quad j = 0, \pm 1, \pm 2, \ldots . \tag{82}$$

The function $x_n(j)$ defines the arrangement of lines in each set and, in general, can be quasiperiodic [104]. In the simplest case it is periodic,

$$x_n(j) = j + \gamma_n. \tag{83}$$

The total set of the lines $\boldsymbol{r}_{n,j}$ forms a grid with fivefold rotational symmetry. Proceeding to the second step, the dual transformation, we map each cell in the grid bounded by the lines $\boldsymbol{r}_{0,j_0}, \boldsymbol{r}_{0,j_0+1}, \ldots, \boldsymbol{r}_{4,j_4}, \boldsymbol{r}_{4,j_4+1}$ to the point

$$\boldsymbol{r} = a_r \sum_{n=0}^{4} j_n \boldsymbol{e}_n \tag{84}$$

belonging to the Penrose lattice. Here a_r is the length of the rhombus side. It has been shown by de Bruijn [100] that the points $\boldsymbol{r}$ form a tiling covering all the plane without empty space provided $\sum_{n=0}^{4} \gamma_n$ is an integer. The canonic Penrose tiling shown in Fig. 30(a) corresponds to $\gamma_n = 2/5$. Its structure factor

$$f(\boldsymbol{q}) = \lim_{N\to\infty} \sum_{j=1}^{N} e^{2i\boldsymbol{q}\boldsymbol{r}_j} = \sum_{h_1 h_2 h_3 h_4} f_{h_1 h_2 h_3 h_4} \delta_{2\boldsymbol{q}-\boldsymbol{G}_{h_1 h_2 h_3 h_4}} \tag{85}$$

illustrated in Fig. 30(b) consists of the Bragg peaks at the 2D diffraction vectors

$$\boldsymbol{G}_{h_1 h_2 h_3 h_4} = G^* \sum_{n=1}^{4} h_n \boldsymbol{e}_n, \quad G^* = \frac{2\pi}{a_r} \times \frac{2\pi\tau^2}{5}. \tag{86}$$

Only four independent integer numbers $h_1, \ldots, h_4$ are sufficient to specify the diffraction vector since $\sum_{n=0}^{4} \boldsymbol{e}_n = 0$. The star of each vector $\boldsymbol{G}$ consists of 10 vectors distributed over two five-vector stars

$$\boldsymbol{G}_{n,\pm} = \pm G \boldsymbol{e}_n, \tag{87}$$

where $n = 0, \ldots, 4$.

The Penrose photonic quasicrystals were first fabricated by the electron beam lithography [18]. Another approach to produce the structure is the optical interference holographic lithography technique [105]. The interference pattern of five coherent beams $\boldsymbol{E}_n \exp(i\boldsymbol{q}_n\boldsymbol{r})$ is given by

$$I(\boldsymbol{r}) = \sum_{n,n'=0}^{4} \boldsymbol{E}_n \cdot \boldsymbol{E}_{n'}^{*} e^{i(\boldsymbol{q}_n - \boldsymbol{q}_{n'})\boldsymbol{r}} \tag{88}$$

and has maxima at the points where $\boldsymbol{r} \cdot (\boldsymbol{q}_n - \boldsymbol{q}_{n'}) = 0, \pm 2\pi, \ldots$. If the wave vectors of the incident beams are chosen as

$$\boldsymbol{q}_n = \frac{G}{\sqrt{4-\tau^2}} \left[\cos\left(\frac{(4n+1)\pi}{10}\right), \sin\left(\frac{(4n+1)\pi}{10}\right)\right], \quad n = 0, \ldots, 4, \tag{89}$$

the differences of the adjacent wave vectors $\boldsymbol{q}_n$ are exactly equal to diffraction vectors (87):

$$\boldsymbol{G}_{n\pm} = \pm(\boldsymbol{q}_{n-1} - \boldsymbol{q}_{n-2}). \tag{90}$$

As a result, the pattern (88) is generally similar to the Penrose lattice and its diffraction image will possess required 10-fold symmetry. Penrose structures in Ref. [105] were fabricated in polymer resin. The polymeric volume fraction was controlled by variation of the beam polarization and exposure dose. This approach can be straightforwardly extended to produce structures with arbitrarily rotational symmetry. Fabrication of quasicrystals with 8-, 10- and 12-fold symmetries is reported in Ref. [106]. An electrically switchable Penrose structure by holographic lithography was realized in Ref. [107]. Two-dimensional photonic quasicrystalline structures with high rotational symmetry, up to 23-fold, as well as 2D Thue–Morse structures are fabricated in Ref. [108]. Finally, 3D icosahedral structures are made in Ref. [35]. The holographic approach in which all elements of the quasicrystalline lattice are fabricated simultaneously is complementary to the direct laser writing technique applied in Ref. [34] where the optical lithography is performed by the tightly focused laser beam.

We note that the dual multigrid technique allows one to establish an interesting relationship between the canonic Penrose tiling and the Fibonacci lattice. It turns out [104] that the Penrose lattice is dual to the pentagrid with the spacings between parallel lines arranged in the Fibonacci sequence. To be precise the function $x_n(j)$ in Eq. (82) must be chosen as

$$x_n(j) = j + \alpha + \frac{1}{\tau}\left\lfloor \frac{j}{\tau} + \beta \right\rfloor \tag{91}$$

with

$$\alpha = \frac{6\tau - 1}{2(\tau+2)}, \quad \beta = -\frac{2}{\tau+2}. \tag{92}$$

Thus, the Penrose tiling can be thought of as a generalization of the Fibonacci lattice to the 2D case.

10.2. Random quasicrystals. Stampfli tilings

Here we discuss a special type of aperiodic structures, random quasicrystals. In Figs. 31(c) and (d) we show examples, respectively, of deterministic and random Stampfli square-triangle tilings [19,109]. The inflation rule for these tilings is broken into four steps.

1. Draw the parent regular dodecagon. Decorate it with square-triangle tiling, as shown in Fig. 31(a).

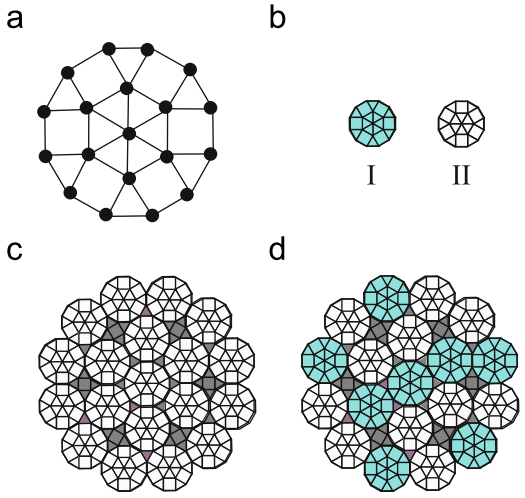

Fig. 31. Illustration of the deterministic [19] and random Stampfli square-triangle tilings [109]. Panel (a) presents parent dodecagon decorated by square-triangle tilings by the way (I). Panel (b) shows two offspring dodecagons with square-triangle decorations of types (I) and (II). The offspring dodecagons are smaller than the parent one by the factor $2+\sqrt{3}$. Panels (c), (d) show iterated deterministic and random tilings, respectively. The structures are obtained by putting the dodecagons (II) (panel c) and the dodecagons (I) or (II) (panel d) in all the vertices of parent dodecagon indicated by dots in panel (a).

2. Scale the parent dodecagon by the factor $1/(2+\sqrt{3})\approx 0.27$ to obtain the offspring dodecagon of type (I). The dodecagon of type (II) is obtained by rotation of the dodecagon (I) by the angle $\pi/6$, see Fig. 31(b). These two dodecagons differ only in their square-triangle decorations, with the middle-top figure in the tiling being either a triangle (I) or a square (II).
3. Place the offspring dodecagons on each vertex of the parent one. By placing the dodecagons of type (II) one obtains the deterministic Stampfli tiling shown in Fig. 31(c). The random distribution of dodecagons (I) and (II) with equal probabilities generates the random Stamfli tiling shown in Fig. 31(d).
4. Repeat the steps 2 and 3 for the structure obtained in the step 3 as a new parental tiling. Note that, for the deterministic tiling, the dodecagon type is changed in each step, i.e., $(\mathrm{I})\to(\mathrm{II})\to(\mathrm{I})\to\cdots$.

Both structures obtained according to this rule are quasicrystalline, i.e., they demonstrate discrete Bragg diffraction pattern [19]. The deterministic structure is a conventional quasicrystal which can be alternatively obtained by the projection from the 4D space. The positions of its diffraction spots have 12-fold rotational symmetry. However, the intensities of the diffraction spots have only 6-fold symmetry reflecting an existence of two inequivalent six-point stars rotated by the angle $\pi/6$ around each other. The randomization procedure used in the generation algorithm for the random Stamfli tiling mixes two stars and doubles the rotational symmetry of the diffraction picture. As a result, the random Stampfli tilings demonstrate macroscopic long-range 12-fold symmetry. This result has been experimentally confirmed by observations of the diffraction pattern from the random photonic quasicrystals [17]. The dodecagonal tiling shown in Fig. 31(a) can serve a basic structural element for many different structures, either periodic or quasiperiodic. Periodic photonic crystals with a compound elementary supercell and the local geometry determined by the tiled dodecagons (I) and (II) have been proposed in Ref. [110]. These highly symmetric structures are termed as Archimedean tilings and serve an alternative to photonic quasicrystals. Other periodic lattices consisting of dodecagons (I) and (II) and having more isotropic Brillouin zones than conventional photonic crystals have been theoretically studied in Ref. [111]. Two-dimensional photonic crystals with octagonal quasicrystalline unit supercells, have been proposed in Refs. [112,113]. Such approximants of ideal quasicrystalline systems also allow to achieve high degree of rotational symmetry of photonic bands.

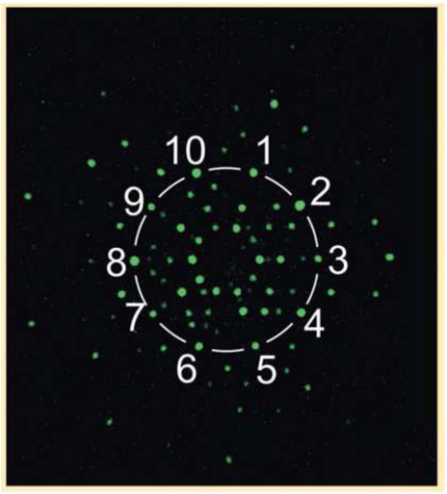

Fig. 32. Measured Laue diffraction pattern of 3D quasicrystal templates using a 532 nm laser. From Ref. [34].

10.3. Three-dimensional icosahedral quasicrystals

Icosahedral quasicrystals present a generalization of Penrose tiling to the 3D space. The cut-and-project algorithm for their generation is sketched below. It is analogous to that discussed in Section 3.1 for the 1D Fibonacci lattice. An icosahedral quasilattice can be constructed by projecting a 6D simple cubic lattice $\boldsymbol{R}_n=\sum_{j=1}^{6} n_j\boldsymbol{a}_j$ onto the 3D space. Here $\boldsymbol{a}_j$ ($j=1,\ldots,6$) are the orthonormal basic vectors of the 6D space, $\boldsymbol{a}_j\cdot\boldsymbol{a}_{j'}=\sum_{l=1}^{6}[\boldsymbol{a}_j]_l[\boldsymbol{a}_{j'}]_l=\delta_{jj'}$ This basis is rotated to obtain another orthonormal basis [114]

$$\boldsymbol{a}_\alpha=\sum_{j=1}^{6} T_{j\alpha}\boldsymbol{a}_j, \tag{93}$$

where $\alpha=x,y,z,x',y',z'$ and the rotation matrix is given by

$$T_{j\alpha}=\frac{1}{\sqrt{2\tau+4}}\begin{pmatrix} \tau & 0 & 1 & \tau & -1 & 0\\ \tau & 0 & -1 & -\tau & -1 & 0\\ 0 & 1 & -\tau & 1 & 0 & \tau\\ -1 & \tau & 0 & 0 & -\tau & -1\\ 0 & 1 & \tau & -1 & 0 & \tau\\ 1 & \tau & 0 & 0 & \tau & -1 \end{pmatrix} \tag{94}$$

and $\tau=(\sqrt{5}+1)/2$ is the golden mean. The 3D set $x\boldsymbol{a}_x+y\boldsymbol{a}_y+z\boldsymbol{a}_z$ defines the physical space E^3, while the orthogonal space $x'\boldsymbol{a}_{x'}+y'\boldsymbol{a}_{y'}+z'\boldsymbol{a}_{z'}$ is called the pseudospace E'^3. The 3D Penrose tiling with the icosahedral symmetry is obtained by taking the 6D lattice vectors $\boldsymbol{R}_n$, which lie inside a unit triacontahedron in the pseudospace, and finding their partial projections on the physical space.

Experimental Laue diffraction pattern of three-dimensional silicon inverse photonic quasicrystals [34] is presented in Fig. 32. High quality of these structures, shown in Fig. 9, is manifested by the diffraction spots with a distinct 10-fold rotational symmetry indicating analogy between the 2D Penrose tiling and the 3D icosahedral lattice, cf. Figs. 30(b) and 32. Further detailed experimental and theoretical study of the transmission spectra

and time-resolved response of silicon inverse icosahedral structures is reported in Ref. [115]. It has been demonstrated that, even for ideal quasicrystals without any disorder or imperfections, the multiple scattering of light in a 3D icosahedral quasicrystal resembles in certain aspects "diffusive" scattering of light in disordered photonic systems. In particular, the calculations [115] indicate that the transmission dependence on the slab thickness L is intermediate between the power law $T \propto 1/L$ holding for disordered systems and the exponential law $\ln T \propto -L$ holding for periodic structures.

11. Nonlinear photonic quasicrystals

A wider variety of photonic quasicrystals as compared to periodic structures means the wider tunability range of their optical properties. This obvious statement is brightly confirmed in nonlinear optics where photonic quasicrystals are very promising for applications. Here, as an example, we consider the third-harmonic generation in solids. Because of a small value of third-order nonlinear susceptibility $\chi^{(3)}$ relating the dielectric polarization $P(3\omega)$ at the third-harmonic frequency with the cube $E^3(\omega)$ of the electric field, the direct generation of the third harmonic is very weak. Instead, a two-step process is much more efficient. It includes the second-order generation, $\omega+\omega=2\omega$, followed by the sum-frequency generation, $2\omega+\omega=3\omega$. Of course the second-order nonlinear susceptibility $\chi^{(2)}$ should be allowed by symmetry and strong enough as in the case of ferroelectric $LiTaO_3$ [117]. However, for a remarkable nonlinear frequency conversion, the both constituent processes require phase matching conditions originating from the momentum conservation law [118]. Chromatic dispersion leads to the nonlinear dependence of the light wave vector on the frequency, $q_\omega = \omega n_\omega/c$, and achievement of phase matching becomes a nontrivial problem. One of the solutions is to use photonic crystals with the diffraction vectors G compensating the momentum mismatch. For the two-step third-harmonic generation, the phase matching conditions read

$$q_{2\omega} = 2q_\omega + G,$$

$$q_{3\omega} = q_\omega + q_{2\omega} + \widetilde{G}. \tag{95}$$

Simultaneous satisfaction of both Eqs. (95) in a *single* photonic crystal is unlikely. Indeed, in a simple 1D lattice with the period d the ratio of the diffraction vectors is rational which leads to the identity

$$\frac{2n_{2\omega}-2n_\omega}{3n_{3\omega}-n_\omega-2n_{2\omega}} = \frac{G}{\widetilde{G}} = \frac{h}{m}, \tag{96}$$

where h and m are integers. Since the left-hand side of Eq. (96) may be arbitrary its rational approximation with adequate precision generally require large values of h and m, which means ineffective diffraction. The two processes (95) can be more effectively realized in two different photonic crystals with unequal periods $d \neq d'$. On the other hand, the both incommensurate periods can be incorporated inside *one* quasicrystalline lattice. For example, for the general binary quasicrystal (1) considered in Section 3.1, with diffraction vectors given by (24), we obtain instead of Eq. (96)

$$\frac{G}{\widetilde{G}} = \frac{h+h'/t}{m+m'/t} \quad (h,h',m,m' = 1,2,3,\ldots). \tag{97}$$

This ratio is controlled by four integers instead of two and an additional free parameter t dependent on the choice of the lattice. Obviously, Eq. (97) can be used for the tuning to the desired value of $G/\widetilde{G}$ much easier which makes quasicrystalline lattices more advantageous in the support of processes (95). Since they occur simultaneously the third-harmonic generation is more efficient than that arising in two successive steps. This elegant approach has been proposed by Zhu et al. in Ref. [116] and realized for a Fibonacci quasicrystal with $t=\tau$ shown schematically in Fig. 33. Each of the layers $\mathcal{A}$ and $\mathcal{B}$ consists of two ferroelectric $LiTaO_3$ domains with opposite directions of the spontaneous polarization. The values of relative domain thicknesses are optimized for an efficient third-harmonic generation. A large number of studies for different 1D structures has been performed since 1997, for more recent developments see Ref. [119] and references therein.

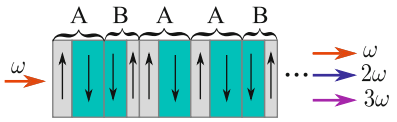

Fig. 33. Schematic illustration of the third-harmonic generation in a ferroelectric Fibonacci structure [116]. Vertical arrows indicate the directions of spontaneous polarization in $LiTaO_3$ domains.

The idea [116] to use quasicrystalline lattices for complex nonlinear optical processes has been extended on the 2D structures in Ref. [120]. The procedure to create a device is generally the same: (i) determine the 2D diffraction vectors for the required nonlinear processes, and (ii) produce the quasiperiodic tiling with the structure factor containing these diffraction vectors. Clearly, the 2D structures provide more opportunities compared to the 1D chains. Chen and Chen [121] have reported the further theoretical generalization, to the 3D case, of the nonlinear quasicrystal construction for given values of the mismatch vectors. In the 3D quasicrystals the design becomes even more flexible.

Nonlinear photonic quasicrystalline structures can be elegantly realized by optical induction technique [122,123] which is generally similar to the optical interference holography discussed in Section 10.1. The intensity pattern arising from the interference of several monochromatic beams is translated into a quasiperiodic modulation of the refractive index of a photorefractive nonlinear material. Typical distance between the lattice sites in such photonic quasicrystal is in order of 10 μm [123]. Only the extraordinary polarized light in $Sr_{0.75}Ba_{0.25}Nb_2O_6$ material used in Ref. [122] experiences an induced spatially varying index of refraction. Hence, if the incident beams have extraordinary polarization, they are affected in turn by the induced index modulation and exhibit complex nonlinear dynamics. Lattice solitons in a quasiperiodic waveguide structure have been observed in Ref. [122] for sufficiently high pump intensities. One of the unique features of quasicrystals is an existence of a specific type of collective excitations, *phasons*, which can be thought of as shifts of the phase of the modulation function $r(j)$ entering Eq. (1). More generally, the phasons are deformations of a periodic lattice in the perpendicular pseudospace in the cut-and-project method [40]. Nonlinear photonic quasicrystalline structures realized in Ref. [123] allow a direct visualization of phason dynamics.

Nonlinear reflectivity of Fibonacci-spaced QWs has been studied in Ref. [10] both experimentally and theoretically. Experimental spectra are taken in a single-beam reflection geometry for varying beam intensities. The theoretical approach involved calculation of the QW susceptibility in the steady state with time-independent carrier densities by numerical solution of semiconductor Maxwell–Bloch equations. Good agreement between experiment and theory is demonstrated by Fig. 34. The spectrum for linear regime, with low pump power (gray area), has been already discussed in Section 9.1 and shown in Fig. 26. It possesses two Bragg peaks at the resonance frequencies of

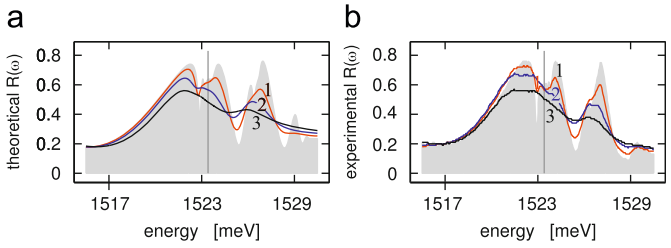

Fig. 34. Computed (a) and experimental (b) nonlinear reflection spectra for Fibonacci QW structures. Theory used the densities $n = 10^9\,\mathrm{cm}^{-2}$ (shaded area), $5\times10^9\,\mathrm{cm}^{-2}$, $2\times10^{10}\,\mathrm{cm}^{-2}$, and $5\times10^{10}\,\mathrm{cm}^{-2}$ (curves 1–3) while in the experiment the pump power was $P=76.6\,\mu\mathrm{W}$ (shaded area), 871 μW, 3.7 and 11.1 mW (curves 1–3). From Ref. [10].

heavy- and light-hole QW excitons. The dip in the middle of the first peak has a fine structure caused by the interference of exciton–polaritons. As the pump-pulse power increases, these sharp exciton–polaritonic spectral features are smeared and the height of Bragg reflectivity peaks declines due to the excitation-induced dephasing. A small reduction in the peak halfwidth, seen in Fig. 34(b), can be interpreted as the saturation of oscillator strength of the excitonic transition.

12. Conclusions

The discovery of quasicrystals and other deterministic aperiodic structures initiated new fields of research in solid-state electronics, phononics and photonics. In this review we have presented recent achievements in fabrication of photonic quasicrystals and, in the main part of the article, tried to span different aspects of the optical spectroscopy of long-range-ordered aperiodic systems and show its current state of the art. We have brought to light nontraditional ways of the structural description of aperiodic photonic systems, including mutually supplementing definitions of binary 1D chains, irrational cuts through higher-dimensional lattices and complete tiling of the 2D and 3D spaces with regular polygons or polyhedrons, respectively.

The studies of quasicrystalline structures have widened the existing concepts of wave diffraction and interference. The light propagating in a structured medium is scattered with the scattering intensity determined by the Fourier transform of a space-dependent function describing the optical response of the medium. We have examined properties of these Fourier transforms, particularly, an existence, distribution and magnitude of the Bragg peaks in the geometrical structure factor.

Emphasis has been placed on similarities and differences between optical properties of this third form of solid matter and those of conventional crystals and amorphous materials. It is shown that, similarly to periodic systems, the two-wave approximation is often efficient to describe, within narrow frequency intervals, the light propagation in quasicrystalline medium. Moreover, sometimes it is even instructive to introduce effective allowed bands and forbidden gaps (or stop-bands) for light waves propagating in such medium. Therefore, we have focused on the two-wave description of light propagation, reflection, transmission, absorption and emission both in nonresonant and resonant structures. An important difference with periodic systems with a simple (undecorated) unit cell is that, in an aperiodic system, the coefficients of the Bragg structure factor differ from unity which has an influence on the gap width and, in the Fibonacci QW structures, leads to formation of an allowed band inside the forbidden gap.

The resemblance to disordered materials reveals in properties of photonic crystalline approximants of quasicrystals. With increasing the thickness of the approximant supercell, the optical spectra provide an evidence for the localization of light waves. The localized states can be analyzed in terms of the participation ratio [124], $p=\sum_{j=1}^{N}|P_j|^4/(\sum_{m=1}^{N}|P_j|^2)^2$, where the sum runs over the lattice sites and, e.g., in multiple quantum wells, P_j is the exciton polarization in the j th well. The analysis of the participation ratio is a convenient method to study localization both in disordered and quasicrystalline systems. We have stressed that important specific features of the latter systems are a scaling and self-similarity of optical spectra which are completely absent in crystalline and amorphous materials.

The peculiar properties of photonic quasicrystals are encouraging for their possible use in optical devices. As one of the most spectacular examples, we have discussed in more detail a high efficiency of phase-matched third-harmonic generation in a quasiperiodic optical superlattice.

Acknowledgments

We thank M.M. Voronov for very fruitful discussions. The support from RFBR, "Dynasty" Foundation-ICFPM, and the National Foundation for Personnel Education is gratefully acknowledged.

Appendix A. General properties of transfer matrices

In this Appendix, by using the transfer matrix approach, we derive the reflection and transmission coefficients for a multilayered system sandwiched between two semi-infinite homogeneous media characterized by the refractive indices n_l and n_r, at $z<0$ and $z>L$, respectively. However, the results can be generalized to an arbitrary 1D structure.

The transfer matrix can be conveniently expressed in the basis of right-propagating (E^+) and left-propagating (E^-) waves

$$E(z)=\begin{cases} E^+_{\mathrm{left}}e^{iq_lz}+E^-_{\mathrm{left}}e^{-iq_lz} & (z<0),\\ E^+_{\mathrm{right}}e^{iq_r(z-L)}+E^-_{\mathrm{right}}e^{-iq_r(z-L)} & (z>L),\end{cases} \tag{A.1}$$

where $q_{r,l}=n_{r,l}\omega/c$. The 2×2 matrix $\hat{M}(n_r,n_l)$ relates the electric field amplitudes by

$$\begin{pmatrix}E^+_{\mathrm{right}}\\ E^-_{\mathrm{right}}\end{pmatrix}=\hat{M}(n_r,n_l)\begin{pmatrix}E^+_{\mathrm{left}}\\ E^-_{\mathrm{left}}\end{pmatrix}. \tag{A.2}$$

The elements of the transfer matrix can be expressed in terms of the reflection coefficients r, $\tilde{r}$ and transmission coefficients t, $\tilde{t}$ corresponding to the initial wave incidence from the left and right sides, as illustrated in Fig. A1. In general, the relation is given by

$$\hat{M}=\frac{1}{\tilde{t}}\begin{pmatrix}t\tilde{t}-r\tilde{r} & \tilde{r}\\ -r & 1\end{pmatrix}. \tag{A.3}$$

For a nonresonant binary chain like that sketched in Fig. 1, it is convenient first to introduce the transfer matrix $\hat{M}(\bar{n},\bar{n})$ for the semi-infinite media with the refractive indices $n_l=n_r=\bar{n}\equiv\sqrt{\bar{\varepsilon}}$. Then the transfer matrix for arbitrary values of n_l and n_r is given by the product

$$\hat{M}(n_r,n_l)=\hat{M}_{\mathrm{int}}(n_r,\bar{n})\times\hat{M}(\bar{n},\bar{n})\times\hat{M}_{\mathrm{int}}(\bar{n},n_l), \tag{A.4}$$

where the transfer matrices through the interfaces read

$$\hat{M}_{\mathrm{int}}(n_2,n_1)=\frac{1}{1-\rho}\begin{pmatrix}1 & -\rho\\ -\rho & 1\end{pmatrix},\quad \rho=\frac{n_1-n_2}{n_1+n_2}. \tag{A.5}$$

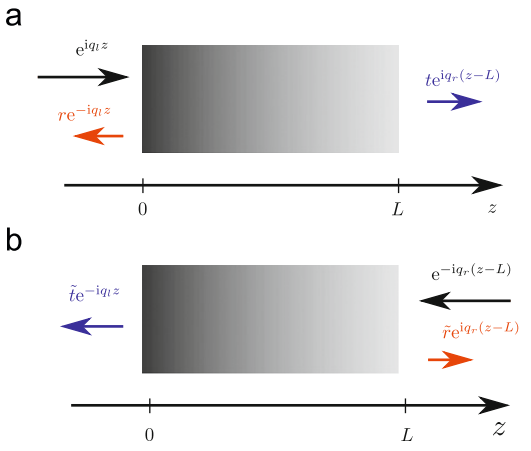

Fig. A1. Definition of reflection coefficients $r, \tilde{r}$ and transmission coefficients $t, \tilde{t}$ of light, incident upon the slab with length L from left (a) and right (b) half-spaces, respectively.

The amplitude reflection and transmission coefficients are finally expressed as

$$r(n_r,n_l) = -\frac{M_{2,1}(n_r,n_l)}{M_{2,2}(n_r,n_l)}, \quad t(n_r,n_l) = -\frac{\det[\hat{M}(n_r,n_l)]}{M_{2,2}(n_r,n_l)}. \tag{A.6}$$

The reflectance and transmittance are found from

$$R = |r(n_r,n_l)|^2, \quad T = n_r|t(n_r,n_l)|^2. \tag{A.7}$$

The transfer matrix $\hat{M}(n,n)$ with coinciding refractive indices $n_l = n_r = n$ is simplified because in this case (in the absence of magnetic fields) the time inversion symmetry imposes the identity $t = \tilde{t}$, even taking into account the absorption inside the layers A and B in which case $\mathrm{Im}\{\varepsilon_{A,B}\} \neq 0$. Moreover, in the particular case of a centrosymmetric structure one has not only $t = \tilde{t}$ but also $r = \tilde{r}$, so that the transfer matrix reduces to

$$\hat{M}(n,n) = \frac{1}{t}\begin{pmatrix} t^2 - r^2 & r \\ -r & 1 \end{pmatrix}. \tag{A.8}$$

On the other hand, if the structure is not absorbing, so that energy conservation law $|t^2| + |r^2| = 1$ holds, the general Eq. (A.3) simplifies to

$$\hat{M}(n,n) = \begin{pmatrix} \dfrac{1}{t^*} & -\dfrac{r^*}{t^*} \\ -\dfrac{r}{t} & \dfrac{1}{t} \end{pmatrix}. \tag{A.9}$$

It should be emphasized that Eqs. (A.8) and (A.9) are independent, the former is applicable for the absorbing symmetric structure and the latter is valid even for noncentrosymmetric one. When the structure is both centrosymmetric and non-absorbing Eqs. (A.8) and (A.9) become identical due to the properties $|t^2| + |r^2| = 1$ and $\mathrm{Re}\{r/t^*\} = 0$.

One can check that the coefficients in Eqs. (A.7) satisfy the energy conservation condition $R + T = 1$ as soon as $\varepsilon_A, \varepsilon_B$ are real. Of course Eqs. (A.4)–(A.7) can also be applied for calculation of optical spectra in the two-wave approximation where the coefficients r and t are given by Eqs. (68).

References

[1] D. Levine, P.J. Steinhardt, Phys. Rev. Lett. 53 (1984) 2477.
[2] M. Kohmoto, B. Sutherland, K. Iguchi, Phys. Rev. Lett. 58 (1987) 2436.
[3] E. Yablonovitch, Phys. Rev. Lett. 58 (1987) 2059.
[4] S. John, Phys. Rev. Lett. 58 (1987) 2486.
[5] E.L. Albuquerque, M.G. Cottam, Phys. Rep. 376 (113) (2003) 225.
[6] W. Steurer, D. Sutter-Widmer, J. Phys. D: Appl. Phys. 40 (2007) R229.
[7] T. Hattori, N. Tsurumachi, S. Kawato, H. Nakatsuka, Phys. Rev. B 50 (1994) 4220.
[8] V. Passias, N.V. Valappil, Z. Shi, L. Deych, A.A. Lisyansky, V.M. Menon, Opt. Express 17 (2009) 6636.
[9] J. Hendrickson, B.C. Richards, J. Sweet, G. Khitrova, A.N. Poddubny, E.L. Ivchenko, M. Wegener, H.M. Gibbs, Opt. Express 16 (2008) 15382.
[10] M. Werchner, M. Schafer, M. Kira, S.W. Koch, J. Sweet, J.D. Olitzky, J. Hendrickson, B.C. Richards, G. Khitrova, H.M. Gibbs, A.N. Poddubny, E.L. Ivchenko, M. Voronov, M. Wegener, Opt. Express 17 (2009) 6813.
[11] B.C. Richards, J. Hendrickson, J. Sweet, G. Khitrova, D. Litvinov, D. Gerthsen, B. Myer, S. Pau, D. Sarid, M. Wegener, E.L. Ivchenko, A.N. Poddubny, H.M. Gibbs, Opt. Express 16 (2008) 21512.
[12] L.D. Negro, M. Stolfi, Y. Yi, J. Michel, X. Duan, L.C. Kimerling, J. LeBlanc, J. Haavisto, Appl. Phys. Lett. 84 (2004) 5186.
[13] A.V. Lavrinenko, S.V. Zhukovsky, K.S. Sandomirski, S.V. Gaponenko, Phys. Rev. E 65 (2002) 036621.
[14] S.V. Gaponenko, S.V. Zhukovsky, A.V. Lavrinenko, K.S. Sandomirskii, Opt. Comm. 205 (2002) 49.
[15] S.V. Zhukovsky, A.V. Lavrinenko, Photonics Nanostructures 3 (2005) 129.
[16] M.A. Kaliteevski, S. Brand, R.A. Abram, T.F. Krauss, P. Millar, R.M. DeLa Rue, J. Phys. Condens. Matter 13 (2001) 10459.
[17] M.E. Zoorob, M.D.B. Charlton, G.J. Parker, J.J. Baumberg, M.C. Netti, Nature 404 (2000) 740.
[18] M.A. Kaliteevski, S. Brand, R.A. Abram, T.F. Krauss, R. DeLa Rue, P. Millar, Nanotechnology 11 (2000) 274.
[19] M. Oxborrow, C.L. Henley, Phys. Rev. B 48 (1993) 6966.
[20] S.-K. Kim, J.-H. Lee, S.-H. Kim, I.-K. Hwang, Y.-H. Lee, S.-B. Kim, Appl. Phys. Lett. 86 (2005) 031101.
[21] K. Nozaki, T. Baba, Appl. Phys. Lett. 84 (2004) 4875.
[22] J.B. Pendry, A.J. Holden, W.J. Stewart, I. Youngs, Phys. Rev. Lett. 76 (1996) 4773.
[23] A.L. Pokrovsky, A.L. Efros, Phys. Rev. B 65 (2002) 045110.
[24] V.G. Veselago, E.E. Narimanov, Nature Mater. 5 (2006) 759.
[25] M. Bayindir, E. Cubukcu, I. Bulu, E. Ozbay, Europhys. Lett. 56 (2001) 41.
[26] M. Bayindir, E. Cubukcu, I. Bulu, E. Ozbay, Phys. Rev. B 63 (2001) 161104.
[27] T.W. Ebbesen, H.J. Lezec, H.F. Ghaemi, T. Thio, P.A. Wolff, Nature 391 (1998) 667.
[28] C. Rockstuhl, F. Lederer, T. Zentgraf, H. Giessen, Appl. Phys. Lett. 91 (2007) 151109.
[29] T. Matsui, A. Agrawal, A. Nahata, Z.V. Vardeny, Nature 446 (2007) 517.
[30] N. Papasimakis, V.A. Fedotov, A.S. Schwanecke, N.I. Zheludev, F.J. García de Abajo, Appl. Phys. Lett. 91 (2007) 081503.
[31] J. Li, S. Liu, C. Huang, T. Li, Q. Wang, Y. Zhu, J. Opt. A: Pure Appl. Opt. 10 (2008) 075202.
[32] A. Gopinath, S.V. Boriskina, B.M. Reinhard, L. Dal Negro, Opt. Express 17 (2009) 3741.
[33] W. Man, M. Megens, P.J. Steinhardt, P.M. Chaikin, Nature 436 (2005) 993.
[34] A. Ledermann, L. Cademartiri, M. Hermatschweiler, C. Toninelli, G.A. Ozin, D.S. Wiersma, M. Wegener, G. von Freymann, Nature Mater. 5 (2006) 942.
[35] J. Xu, R. Ma, X. Wang, W.Y. Tam, Opt. Express 15 (2007) 4287.
[36] M.H. Kok, W. Lu, W.Y. Tam, G.K.L. Wong, Opt. Express 17 (2009) 7275.
[37] A. Ledermann, G. von Freymann, M. Wegener, Physik in unserer Zeit 38 (2007) 300.
[38] M.Y. Azbel, Sov. Phys. JETP 19 (1964) 634.
[39] M.Y. Azbel, Phys. Rev. Lett. 43 (1979) 1954.
[40] C. Janot, Quasicrystals. A Primer, Clarendon Press, Oxford, UK, 1994.
[41] Z. Lin, M. Goda, H. Kubo, J. Phys. A 28 (1995) 853.
[42] J.M. Luck, C. Godreche, A. Janner, T. Janssen, J. Phys. A 26 (1993) 1951.
[43] X. Fu, Y. Liu, P. Zhou, W. Sritrakool, Phys. Rev. B 55 (1997) 2882.
[44] M. Kolář, Phys. Rev. B 47 (1993) 5489.
[45] E.L. Ivchenko, A.I. Nesvizhskii, S. Jorda, Phys. Solid State 36 (1994) 1156.
[46] A.N. Poddubny, L. Pilozzi, M.M. Voronov, E.L. Ivchenko, Phys. Rev. B 77 (2008) 113306.
[47] M.C. Valsakumar, V. Kumar, Pramana 26 (1986) 215.
[48] Z. Lin, H. Kubo, M. Goda, Z. Phys. B: Cond. Matter 98 (1995) 111.
[49] M. Goda, H. Kubo, J. Phys. Soc. Japan 58 (1989) 3624.
[50] M. Goda, T. Takemori, H. Kubo, T. Ogawa, J. Phys. Soc. Japan 59 (1990) 3977.
[51] S. Chattopadhyay, A. Chakrabarti, Phys. Rev. B 65 (2002) 184204.
[52] P. Tong, Phys. Rev. B 53 (1996) 1795.
[53] X.Q. Huang, S.S. Jiang, R.W. Peng, A. Hu, Phys. Rev. B 63 (2001) 245104.
[54] A. Chakrabarti, S.N. Karmakar, Phys. Rev. B 44 (1991) 896.
[55] A. Thue, Norske Vididensk. Selsk. Skr. 7 (1906) 1.
[56] M. Morse, Amer. J. Math. 43 (1921) 35.
[57] Z. Cheng, R. Savit, R. Merlin, Phys. Rev. B 37 (1988) 4375.
[58] C.S. Ryu, G.Y. Oh, M.H. Lee, Phys. Rev. B 46 (1992) 5162.
[59] C.S. Ryu, G.Y. Oh, M.H. Lee, Phys. Rev. B 48 (1993) 132.
[60] S. Tamura, F. Nori, Phys. Rev. B 40 (1989) 9790.
[61] N.h. Liu, Phys. Rev. B 55 (1997) 3543.
[62] S. Chattopadhyay, A. Ghosh, A. Chakrabarti, Phys. Rev. B 63 (2001) 064201.
[63] L. Moretti, V. Mocella, Opt. Express 15 (2007) 15314.
[64] H. Lei, J. Chen, G. Nouet, S. Feng, Q. Gong, X. Jiang, Phys. Rev. B 75 (2007) 205109.
[65] V. Agarwal, J. Soto-Urueta, D. Becerra, M.E. Mora-Ramos, Photonics Nanostructures Fund. Appl. 3 (2005) 155.

[66] M.S. Vasconcelos, P.W. Mauriz, F.F. de Medeiros, E.L. Albuquerque, Phys. Rev. B 76 (2007) 165117.
[67] H. Aynaou, V.R. Velasco, A. Nougaoui, E.H.E. Boudouti, D. Bria, Superlattices Microstructures 32 (2002) 35.
[68] D. Levine, P.J. Steinhardt, Phys. Rev. B 34 (1986) 596.
[69] C. Kittel, Introduction to Solid State Physics, Wiley, New York, 1996.
[70] M.W.C. Dharma-wardana, A.H. MacDonald, D.J. Lockwood, J.-M. Baribeau, D.C. Houghton, Phys. Rev. Lett. 58 (1987) 1761.
[71] E. Liviotti, J. Phys.: Condens. Matter 8 (1996) 5007.
[72] L.I. Deych, D. Zaslavsky, A.A. Lisyansky, Phys. Rev. E 56 (1997) 4780.
[73] M.A. Kaliteevski, V.V. Nikolaev, R.A. Abram, S. Brand, Opt. Spectroscopy 81 (2001) 109.
[74] L.D. Negro, J.H. Yi, V. Nguyen, Y. Yi, J. Michel, L.C. Kimerling, Appl. Phys. Lett. 86 (2005) 261905.
[75] J. Brehm, Z. Phys. B: Cond. Matter 85 (1991) 145.
[76] M. Kolář, M.K. Ali, Phys. Rev. A 42 (1990) 7112.
[77] X. Wang, U. Grimm, M. Schreiber, Phys. Rev. B 62 (2000) 14020.
[78] F. Qiu, R.W. Peng, X.Q. Huang, Y.M. Liu, M. Wang, A. Hu, S.S. Jiang, Europhysics Lett. 63 (2003) 853.
[79] P. Mauriz, M. Vasconcelos, E. Albuquerque, Phys. Lett. A 373 (2009) 496.
[80] V.P. Bykov, Soviet J. Exp. Theor. Phys. 35 (1972) 269.
[81] P. Lodahl, A. Floris van Driel, I.S. Nikolaev, A. Irman, K. Overgaag, D. Vanmaekelbergh, W.L. Vos, Nature 430 (2004) 654.
[82] L.I. Deych, M.V. Erementchouk, A.A. Lisyansky, E.L. Ivchenko, M.M. Voronov, Phys. Rev. B 76 (2007) 075350.
[83] S.V. Deshpande, E. Gulari, S.W. Brown, S.C. Rand, J. Appl. Phys. 77 (1995) 6534.
[84] S.V. Boriskina, A. Gopinath, L.D. Negro, Physica E: Low-dimensional Systems and Nanostructures 41 (2009) 1102 Proceedings of the E-MRS 2008 Symposium C: Frontiers in Silicon-Based Photonics.
[85] A.S. Sánchez, P. Halevi, Phys. Rev. E 72 (2005) 056609.
[86] F. de Medeiros, E. Albuquerque, M. Vasconcelos, G. Farias, Surface Sci. 600 (2006) 4337.
[87] E. Ivchenko, Excitons, in: E.I. Rashba, M.D. Sturge (Eds.), Modern Problems in Condensed Matter Science, vol. 2, North-Holland, Amsterdam, 1982.
[88] E.L. Ivchenko, G. Pikus, Superlattices and other Heterostructures: Symmetry and Optical Phenomena, Springer-Verlag, Berlin, 1997.
[89] A.N. Poddubny, L. Pilozzi, M.M. Voronov, E.L. Ivchenko, Phys. Rev. B 80 (2009) 115314.
[90] E.L. Ivchenko, Optical Spectroscopy of Semiconductor Nanostructures, Alpha Science International, Harrow, UK, 2005.
[91] M. Kohmoto, J.R. Banavar, Phys. Rev. B 34 (1986) 563.
[92] M. Kohmoto, Y. Oono, Phys. Lett. 102A (1984) 145.
[93] M. Kohmoto, B. Sutherland, C. Tang, Phys. Rev. B 35 (1987) 1020.
[94] L.D. Negro, N.-N. Feng, Opt. Express 15 (2007) 14396.
[95] C. Forestiere, G. Miano, G. Rubinacci, L.D. Negro, Phys. Rev. B 79 (2009) 085404.
[96] C. Forestiere, G. Miano, C. Serpico, M. d'Aquino, L.D. Negro, Phys. Rev. B 79 (2009) 214419.
[97] J. Dong, K.H. Fung, C.T. Chan, H. Wang, Phys. Rev. B 80 (2009) 155118.
[98] R. Penrose, Bull. Inst. Math. Appl. 10 (1974) 266.
[99] W. Steurera T. Haibacha, International Tables for Crystallography, volume B (Chapter 4.6). Reciprocal-space images of aperiodic crystals, International Union of Crystallography, 2006.
[100] N. de Bruijn, Nederl. Akad. Wetensch. Indag. Math. 43 (1981) 39.
[101] F. Gahler, J. Rhyner, J. Phys. A: Math. General 19 (1986) 267.
[102] P. Gummelt, Geom. Dedicata 62 (1996) 1.
[103] K.N. Ishihara, A. Yamamoto, Acta Cryst. A 44 (1988) 508.
[104] J.E.S. Socolar, P.J. Steinhardt, Phys. Rev. B 34 (1986) 617.
[105] X. Wang, C. Ng, W. Tam, C. Chan, P. Sheng, Adv. Matter 15 (2003) 1526.
[106] R. Gauthier, A. Ivanov, Opt. Express 12 (2004) 990.
[107] S.P. Gorkhali, J. Qi, G.P. Crawford, Appl. Phys. Lett. 86 (2005) 011110.
[108] G. Zito, B. Piccirillo, E. Santamato, A. Marino, V. Tkachenko, G. Abbate, Opt. Express 16 (2008) 5164.
[109] F. Gahler, R. Klitzing, The diffraction pattern of self-similar tilings, in: R.V. Moody (Ed.), The Mathematics of Long-Range Aperiodic Order, NATO series, Kluwer Academic Publishers, Dordrecht, 1997, pp. 141–174.
[110] S. David, A. Chelnokov, J.-M. Lourtioz, Opt. Lett. 25 (2000) 1001.
[111] S.-C. Cheng, X. Zhu, S. Yang, Opt. Express 17 (2009) 16710.
[112] D.T. Roper, D.M. Beggs, M.A. Kaliteevski, S. Brand, R.A. Abram, J. Modern Opt. 53 (2006) 407.
[113] D.M. Beggs, M.A. Kaliteevski, R.A. Abram, J. Modern Opt. 54 (2007) 881.
[114] F.H. Li, L.C. Wang, J. Phys. C: Solid State Phys. 21 (1988) 495.
[115] A. Ledermann, D.S. Wiersma, M. Wegener, G. von Freymann, Opt. Express 17 (2009) 1844.
[116] S. Zhu, Y. Zhu, N. Ming, Science 278 (1997) 843.
[117] Y.R. Shen, Principles of Nonlinear Optics, Wiley, New York, 1984.
[118] L. Landau, E. Lifshitz, Electrodynamics of Continuous Media, Pergamon, New York, 1974.
[119] Y. Qin, C. Zhang, D. Zhu, Y. Zhu, H. Guo, G. You, S. Tang, Opt. Express 17 (2009) 11558.
[120] R. Lifshitz, A. Arie, A. Bahabad, Phys. Rev. Lett. 95 (2005) 133901.
[121] J. Chen, X. Chen, Phys. Rev. A 80 (2009) 013801.
[122] B. Freedman, G. Bartal, M. Segev, R. Lifshitz, D.N. Christodoulides, J.W. Fleischer, Nature 440 (2006) 1166.
[123] B. Freedman, R. Lifshitz, J.W. Fleischer, M. Segev, Nature Mater. 6 (2007) 776.
[124] N. Zekri, A. Brezini, Phys. Stat. Sol. (b) 169 (1992) 253.